12-14-2018

Hypervelocity Impact Experimentation of a Novel Micrometeoroid/Orbital Debris Shielding Concept Imbibed with Rheologically Characterized Shear Thickening Fluids

Justin Marshall Warren

Hypervelocity impact experimentation of a novel micrometeoroid/orbital debris shielding concept imbibed with rheologically characterized shear thickening fluids

By

Justin Marshall Warren

A Dissertation
Submitted to the Faculty of
Mississippi State University
in Partial Fulfillment of the Requirements
for the Degree of Doctor of Philosophy
in Aerospace Engineering
in the Department of Aerospace Engineering

Mississippi State, Mississippi

December 2018

Hypervelocity impact experimentation of a novel micrometeoroid/orbital debris shielding concept imbibed with rheologically characterized shear thickening fluids

By

Justin Marshall Warren

Approved:

_____

Thomas E. Lacy, Jr.
(Major Professor)

_____

Santanu Kundu
(Co-Major Professor)

_____

Keith Koenig
(Committee Member)

_____

Charles U. Pittman, Jr.
(Committee Member)

_____

David S. Thompson
(Graduate Coordinator)

_____

Jason M. Keith
Dean
Bagley College of Engineering

Name: Justin Marshall Warren

Date of Degree: December 14, 2018

Institution: Mississippi State University

Major Field: Aerospace Engineering

Major Professors: Dr. Thomas E. Lacy, Jr. and Dr. Santanu Kundu

Title of Study: Hypervelocity impact experimentation of a novel micrometeoroid/orbital debris shielding concept imbibed with rheologically characterized shear thickening fluids

Pages in Study 92

Candidate for Degree of Doctor of Philosophy

Spacecraft are vulnerable to hypervelocity impacts (HVIs) from micrometeoroid/orbital debris (MMOD) while in space and must mitigate these using shielding. In this research aluminum honeycomb core sandwich panels filled with a shear thickening fluid (STF) were developed as a novel MMOD shielding concept. STFs display a marked rise in viscosity with increasing shear rate above a critical shear rate. The results of HVI experiments with impact velocities of ~4.8 km/s or ~6.8 km/s at -80^{o}C or 21^{o}C showed that incorporating a STF into shielding, as opposed to the STF's liquid phase alone, can reduce damage to the core and the likelihood of back-side facesheet perforation in the event of HVI.

STFs can be subjected to a significant temperature variation in many applications such as the HVI experiments in this research or when deployed on the surface of a spacecraft. The effect of temperature on the shear-thickening behavior was investigated using four low molecular weight polymeric glycols/fumed-silica suspensions. The dispersed phase volume-fraction, its surface chemistry, and the chemical compositions of the suspending media were varied in a series of steady shear rheological characterizations

over a range of temperatures. It was thought that hydroclustering mechanism initiated the onset of shear thickening, and this onset was shown to be more closely correlated to a critical shear rate rather than a critical shear stress.

Evidence of the hydroclustering mechanism was sought using small angle neutron scattering (SANS) experiments. SANS steady state rheological characterization experiments were carried out on five low molecular weight polymeric glycols/fumed-silica STFs at the NIST Center for Neutron Research. The SANS experiments were conducted at shear rates below the critical shear rates, at the critical shear rates, and during shear thickening. In all the SANS experiments, the results showed an increase in scattering intensity with increasing shear rates indicating an evolution of the suspension microstructure consistent with the formation of hydroclusters.

Keywords: HVI, MMOD shielding, STF, rheological characterization, SANS

ACKNOWLEDGEMENTS

This Doctor of Philosophy will be my third degree from Mississippi State University covering the last thirteen years. Many people along the way have either helped me or significantly influenced my understanding of engineering or both. I'd like to acknowledge Jim Schrock who gave me my first job on campus working in Patterson lab as an undergraduate and taught me hands on shop skills that have served me well. Dr. Lacy gave me my second job as an undergraduate performing mechanical testing on auto glass at CAVS. I appreciated and enjoyed the opportunity to work for Dr. Lacy and Dr. Hwang in the lab. I gained valuable experience in many areas including mechanical testing, data acquisition, and strain gage application.

As I'm sure any ASE undergraduate would attest, Dr. Koenig is most likely one of their favorite professors notable for his unique way of explaining just about anything and his dry sense of humor. Whenever I have asked him a question in his office, the response is always the same. He is very calm and contemplative for a few moments, maybe pulling a book off the shelf or a file up on the computer, and then he lays out a satisfying discussion of the explanation to the question. Spacecraft propulsion was my favorite undergraduate course, and I enjoyed relearning the material for my qualifying exams.

I very much appreciate Dr. Lacy's invitation to join the research group when I returned to ASE to be a lecturer. Early on, he encouraged me to look for research

opportunities involving the gas gun, to apply for fellowships, and to transition from a lecturer to a PhD student, which was probably the best career advice I have ever received. I not only appreciated Dr. Lacy's general optimism, leadership of the research group, and teaching style, which I tried to emulate when I taught sections of Mechanics of Materials, but also the many discussions of current political and economic affairs. Two of my favorite graduate courses were Continuum Mechanics and Composites, not only for their content, but also for the engagement Dr. Lacy fostered in the classroom.

Dr. Kundu and Dr. Pittman are also worthy of acknowledgement. I thank Dr. Kundu for his support in the lab, his ideas for experiments and research directions, and the opportunities he facilitated, the most impressive of which was working with the research nuclear reactor at the NIST Center for Neutron Research, not once but twice. Those were surreal experiences. I also thank Dr. Pittman for his dogged persistence in forcing me to think more deeply about my research. His inquisitiveness knows no bounds. You really know you stuff if you can answer a question to Dr. Pittman's satisfaction.

I am also grateful for the help of student members of the research group. Sean Offenberger and Christian Mihigo proved to be well adapted to producing shear thickening fluids with good consistency. I also must thank Kalyan Raj Kota for his friendship and help in the lab and the shop and for teaching me to cook Indian cuisine.

Lastly I am grateful for the chance to work with Dr. Newman Jr. Fracture Mechanics and Fatigue in Metals were my other two favorite graduate courses. They were a unique opportunity to take courses on concepts that the professor either had a hand in forming or knows personally the individuals that did. I am very proud of the

many times Dr. Newman asked me to apply strain gages to his fatigue specimens and of the opportunity to help him publish an article validating his Two-Parameter Fracture Criterion.

TABLE OF CONTENTS

LIST OF TABLES

LIST OF FIGURES

CHAPTER I

INTRODUCTION

1.1 Shear Thickening Fluid Background

Shear thickening fluids (STFs) stand apart from other suspensions due to their remarkable shear rate and temperature dependent viscosity. This work investigated the shear rate and temperature dependent behavior and microstructure of STFs as well as explore a novel application of STFs in a spacecraft shielding concept for micrometeoroid/ orbital debris (MMOD) hypervelocity impact (HVI) mitigation. The resulting HVI experiments showed that the incorporation of STF, as opposed to its liquid phase alone, into a porous core sandwich structure reduced the extent of core damage and rear facesheet perforation.

Consider Figure 1.1 taken from Wagner and Brady 2009, which shows the basic nature of a STF's shear rate dependent viscosity.[1] Repulsive forces, which might include Brownian or electrostatic effects, determine the equilibrium microstructure of the suspended particles when no shear rate is being applied. The middle portion of Figure 1.1 shows shear thinning behavior where at low applied shear rates the STF's viscosity will decrease with increasing shear rate. During shear thinning the particles will align so as to pass each other more easily in the flow. However, once a critical shear rate is reached the fluid will shear thicken wherein the viscosity will increase with increasing shear rates, which is depicted in the right portion of Figure 1.1 This increase in viscosity

is often both dramatic and nearly discontinuous and is caused by the formation of local density variations of particles known as hydroclusters. The rheological characterizations of the STFs in this work show evidence that the hydroclustering mechanism causes the onset of the shear thickening phenomenon.

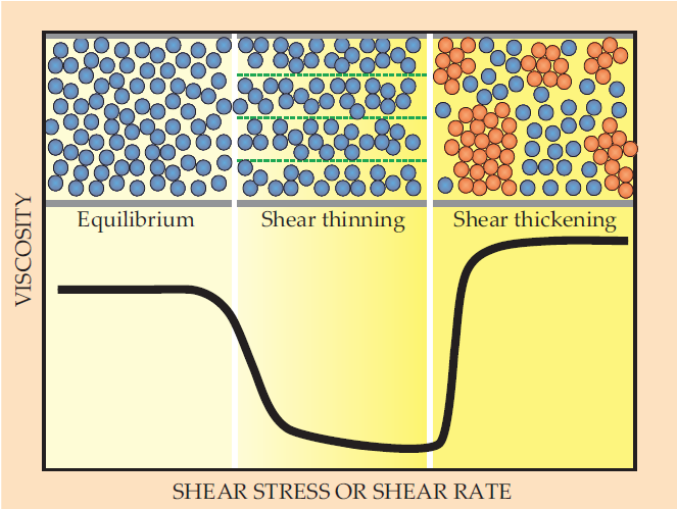

Figure 1.1 Shear rate dependent viscosity

Representative shear rate dependent viscosity of a STF showing the initial equilibrium microstructure, the alignment mechanism during shear thinning, and the hydroclustering mechanism during shear thickening[1]

Interest in the rheological behavior of dense particulate suspensions under applied shear rates can be traced back to the work of Reynolds.[2] In 1885, he documented the curious behavior of densely packed granular suspensions when a shear rate was applied, in this case sand and water. The surface seemed to become dry because the packing orientation of the particles was rearranged causing the fluid to retreat into the increased interstitial spaces of the dilated packing orientation. Reynolds was also the first to use

the word dilatancy to describe this phenomenon. The shear rate dependent behavior of very dilute particulate suspensions were investigated by Einstein in 1906.[3] However, the particulate volume fraction of these suspensions was so low as to preclude particle interaction during shear.[3]

Interest continued with the work of such researchers as Bagnold and Metzner in the 1950's.[4,5] Both used a Couette geometry rheometer to investigate the shear rate dependent behavior of particulate suspensions when the volume fraction of the particles was varied as well as the base viscosity of the suspending fluid.[4,5] But as Barnes noted in his 1989 state of the art review, only about 100 articles had been written over the hundred years since Reynolds' experiments.[6] However, research involving STFs has greatly increased since 1989.

The experimental characterization of STF behavior has recently been extended from rheometers, whether rotational or extensional, to small angle neutron scattering (SANS) experiments that can probe the particulates' microstructural evolution more directly and at the scale of not only the suspended particles but also the roughness of their surfaces.[7,8] The modern era of STF characterization has also tended to investigate the beneficial characteristics of STFs when used in novel applications. Lee et al. impregnated aramid fiber soft-body armor with a STF to improve its ballistic impact resistance by changing the energy absorption mechanism from fiber pullout and yielding to fiber breakage.[9] Fischer et al. employed a STF to dampen the vibration of alpine skies.[10] Recently, imbibing porous core sandwich panel spacecraft shielding concepts has recently shown promise for mitigating HVI of MMOD.[11]

1.2 Micrometeoroid/ Orbital Debris Background

MMOD are a major concern for spacecraft operating in the near-Earth space environment because these high energy impacts of particles on the scale of approximately 1 mm in diameter will inevitably occur for missions of any significant duration.[12] Micrometeoroids are small-scale naturally occurring debris originating from comets and asteroids.[12,13] Micrometeoroids usually have masses of less than 1g but can reach velocities up to 72 km/s with an average velocity of 19 km/s.[12,13] Orbital debris are manmade objects in orbit around the earth resulting from either collisions or discarded remnants of past space missions that serve no longer useful function. They have an average velocity of 8 km/s but can reach 14 km/s.[12,13] The amount of orbital debris is continually increasing, especially in the orbits which are most commonly utilized.[12,13] Since such impacts will inevitably occur, MMOD impact mitigation is a crucial aspect in the design of space structures, especially those meant for human habitation.

The first concept for mitigating MMOD impacts was proposed by Whipple in 1947 and consisted of a single, thin aluminum shielding layer placed at some standoff distance away from the spacecraft hull.[14] Several notable MMOD shielding configurations have been developed since then including the multi-shock concept,[15] the mesh double bumper,[16] and the stuffed Whipple shield.[17] These all feature sacrificial layers outside of the spacecraft structural hull with standoff distances between each layer. Depending on the impact pressure generated, each shielding layer will fracture, melt, or vaporize the incoming projectile as well as portions of the shield local to the point of impact; this forms a debris cloud.[18] The standoff distance allows the debris cloud to expand as it moves toward the next layer, thereby dispersing its energy over a larger area

of the neighboring layer. The use of MMOD shielding based on standoff distances has shown to be effective, but the standoff distances do take up very valuable space. The HVI experiments in this work investigated the possibility of incorporating a MMOD shielding concept within a structural component that might also add other multifunctional qualities.

CHAPTER II

HYPERVELOCITY IMPACT OF HONEYCOMB CORE SANDWICH PANELS IMBIBED WITH SHEAR THICKENING FLUID

2.1 Introduction

Micrometeoroid/orbital debris (MMOD) impacts are a major concern for spacecraft operating in the near-Earth space environment due to their high velocities. These high energy impacts of small particles (~1 mm in diameter) will inevitably occur for missions of any significant duration.[12] Micrometeoroids are small-scale naturally occurring debris originating from comets and asteroids.[12,13] Micrometeoroids usually have masses of less than 1 g but can reach velocities of up to 72 km/s with an average velocity of 19 km/s.[12,13] Orbital debris are manmade objects in orbit around the earth resulting from either collisions or discarded remnants of past space missions that serve no useful function, and they have an average velocity of 8 km/s but can reach 14 km/s. [12-13] The amount of orbital debris is continually increasing, especially in the orbits which are most commonly utilized. [12-13] Since such impacts will occur, MMOD impact mitigation is a crucial aspect in the design of space structures, especially those meant for human habitation.

The first concept for mitigating MMOD impacts was proposed by Whipple in 1947 and consisted of a single, thin aluminum shielding layer placed at some standoff distance away from the spacecraft hull.[14] Several notable MMOD shielding configurations have since been developed, including the multi-shock concept, the mesh

double bumper, and the stuffed Whipple shield.[15-17] These all feature sacrificial layers outside of the spacecraft structural hull with standoff distances between each layer. Depending on the impact pressure generated, each shielding layer will fracture, melt, or vaporize the incoming projectile as well as portions of the shield local to the point of impact; this forms a debris cloud.[18] The standoff distance allows the debris cloud to expand as it moves toward the next layer in the stack up, thereby dispersing its energy over a larger area of the adjacent layer. However, an interesting phenomenon occurs when a honeycomb core sandwich panel is impacted. The honeycomb cell walls have a tendency to restrict the expansion of the debris cloud resulting in far greater damage to the back-side facesheet due to more concentrated debris impacting a smaller area of the back-side facesheet.[19]

Because a spacecraft must fit inside its launch vehicle, sacrificial MMOD shielding with many layers can take up valuable volume inside the launch vehicle as well as add weight. Therefore, MMOD shielding that is integral to the spacecraft hull could prove advantageous. In this study, the aluminum honeycomb core of aluminum facesheet sandwich panels was filled with either a shear thickening fluid (STF) or the STF's liquid phase and subjected to hypervelocity impact (HVI) experiments to explore the effectiveness of using a STF as part of an integral shielding. STFs have unique shear-rate and temperature dependent viscosities and have been used in novel ways to take advantage of this property. Bulletproof vests impregnated with a STF show a marked increase in impact resistance, and a STF has also been shown capable of damping the vibration in alpine skies.[9-10] Here HVI experiments of the STF-filled panels were performed at two different temperatures ($T_1 \approx 21°C$, $T_2 \approx -80°C$) and impact velocities

($V_1 \approx 6.8$ km/s, $V_2 \approx 4.8$ km/s). It was shown that damage done to the facesheets and core was considerably less for panels filled with the STF as opposed to being filled with the STF's liquid phase alone. The method of panel construction was also shown to affect the HVI outcomes.

2.2 Materials

2.2.1 Shear Thickening Fluid

STFs stand apart from other suspensions due to their remarkable shear-rate and temperature dependent viscosity.[1] A STF is composed of a solid particulate phase suspended in a liquid continuous phase. The STF in this study was 0.3 mass fraction (MF) hydrophilic Aerosil 200 fumed silica (A200 silica) suspended in 200 g/mol molecular weight polar polyethylene glycol (PEG). The A200 silica particles are fractal-like branched aggregates that measure approximately 120 nm in characteristic length, and their hydrophilic surface chemistry allowed them to be readily suspended in the polar PEG. The panels subjected to HVIs in this investigation were filled with either the STF or the STF's liquid phase, PEG, the choice of which affected the panel's impact mitigation capability. The PEG filled panels sustained notably greater amounts of damage to the core and facesheets than the STF filled panels.

Figure 2.1 shows the measured shear rate versus viscosity from steady shear rheological tests of the 0.3 MF A200 silica in PEG STF over a small range in temperature (0°C-40°C). Warren et al. have characterized the shear rate and temperature dependent behavior of similar STFs.[20] The characterizations were performed on a TA Instruments DH-2 rheometer using 25 mm parallel plate fixtures and a 1 mm gap. The fluid viscosity initially decreases with increasing shear rate, or "shear thins," as the STF's equilibrium

microstructure is broken up and particles realign to move past each other in the flow. However, at some critical shear rate the viscosity increases with increasing shear rate, or "shear thickens." Here, hydroclusters begin to form wherein particles stay in close proximity when they approach each other. Simulations show that the size and number of hydroclusters increases with increasing shear rates.[21] The nature of the shear thinning region, shear thickening region, and critical shear rate can be tailored by varying parameters such as the size and shape of the particles, the particles' surface chemistry and their interaction with the liquid, the MF of particles, etc.

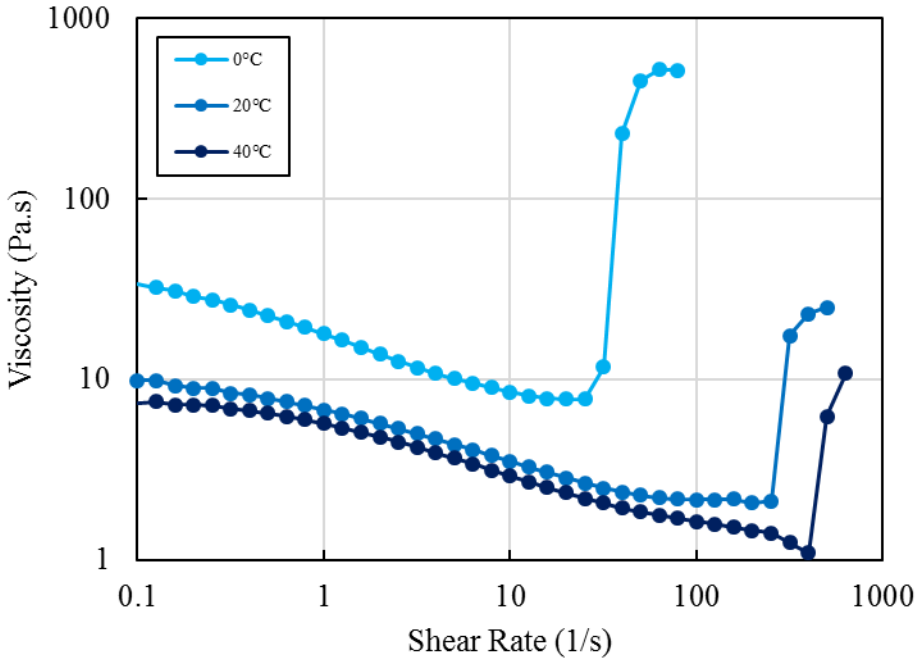

Figure 2.1 Shear thickening behavior

Shear rate versus viscosity results for 0.3 mass fraction Aerosil 200 fumed silica suspended in 200 g/mol molecular weight polyethylene glycol over a temperature range of 0°C-40°C.

In general, the STF viscosity can decrease significantly with increasing temperature. Also, the magnitude of the viscosity increase during shear thickening increases with decreasing temperature. The extent of damage resulting from the HVIs in this investigation showed a significant dependence on temperature.

2.2.2 Aluminum Sandwich Panels

Ten identical 10.16 cm x 10.16 cm x 1.40 cm sandwich panels were constructed using 0.064 cm thick 6061-T6 aluminum front and back-side facesheets separated by 1.27 cm thick 5056 Hexcel hexagonal aluminum honeycomb (0.48 cm cell size and 0.025 mm foil gauge). A moisture resistant 3M AF-163-2U film adhesive was used to bond the facesheets to the core. Eight panels were filled with the 0.3 MF A200 in PEG STF, and two panels were filled with the STF's liquid phase only, PEG.

Assembly of the sandwich panels consisted of three steps. 1) Using an autoclave the honeycomb core was bonded to a single facesheet at 121.1^{o}C and 0.172 MPa for 60 min. 2) After curing the bottom facesheet to the core, a central portion of the honeycomb cells was filled with either the STF or PEG. 3) The second facesheet was bonded to the liquid filled honeycomb core at 107.2^{o}C and 0.172 MPa for 90 min. The soaking temperatures and curing times for step 3 were different from those in step 1 in order not to degrade the first facesheet adhesive's bond.

The facesheet in step 1 that was cured dry will be referred to as Facesheet 1. The facesheet in step 3 that was cured while in the presence of a fluid, whether the STF or PEG, will be referred to as Facesheet 2. It will be evident later that a portion of the adhesive for Facesheet 2 flowed during the second cure into the STF or PEG, thus reducing the mass of adhesive present in the bond line between the core and Facesheet 2

and lowering the second facesheet's bond strength. Also, it has recently been suggested that at high temperatures, such as used in the cure cycles for these panels, the STF employed here might change from a liquid to a somewhat gel-like state.[22]

2.3 Hypervelocity Impact Tests

All targets were subjected to HVI experiments at the light gas gun facility at the University of Kent, Canterbury.[23] Four of the STF-filled panels along with the two PEG-filled panels were impacted at room temperature ($T_1 \approx 21°C$), and four STF-filled panels were impacted at a nominal temperature of $T_2 \approx -80°C$ where the STF was frozen. At both temperatures, two STF-filled panels were impacted at a higher velocity ($V_1 \approx$ 6.8 km/s), and two at a lower velocity ($V_2 \approx 4.8$ km/s). The two PEG-filled panels were impacted at room temperature ($T_1 \approx 21°C$) at the higher velocity ($V_1 \approx 6.8$ km/s). The PEG-filled panels sustained greater damage to the core and facesheets than the STF-filled panels. The back-side facesheet of one of the PEG-filled panels was even perforated by a projectile, which were 1 mm diameter 420 stainless steel spheres. None of the back-side facesheets of the STF-filled panels were perforated. Table 2.1 lists the target temperature, impact velocity, and kinetic energy for each experiment. The Impacted Facesheet column of Table I refers to whether Facesheet 1 or Facesheet 2 was impacted. Note in Table 2.1 that only two panels were imbibed with PEG instead of the STF.

Table 2.1 Experimental data for impacted targets

	Target Number	Impacted Facesheet	Imbibed Liquid	Temp (°C)	Velocity (km/s)	Kinetic Energy (J)	Back-side Facesheet Perforated
Room Temperature	1	2	PEG	21	6.85	95.4	Yes
	2	2	STF	21	6.83	94.5	No
	3	1	PEG	21	6.86	95.1	No
	4	1	STF	21	6.81	94	No
	5	1	STF	21	4.94	49.4	No
	6	2	STF	21	4.7	44.8	No
Lower Temperature	7	1	STF	-75.8	6.82	94.2	No
	8	2	STF	-86	6.82	94.2	No
	9	1	STF	-84.8	4.91	48.9	No
	10	2	STF	-85.4	4.74	45.5	No

2.4 Results and Discussion

X-ray computerized tomography (CT) scans were performed on the impacted specimens to inspect internal damage taking a scan at 0.5 mm intervals. Figure 2.2 shows the rendered CT images of the STF-filled and PEG-filled panels impacted at room temperature ($T_1 \approx 21°C$) at the higher velocity ($V_1 \approx 6.8$ km/s). These conditions were capable of producing the greatest amount of damage in this study. Facesheet 2 was the

impact-side facesheet for both of these. The only difference between these two panels is which liquid the honeycomb core was filled with.

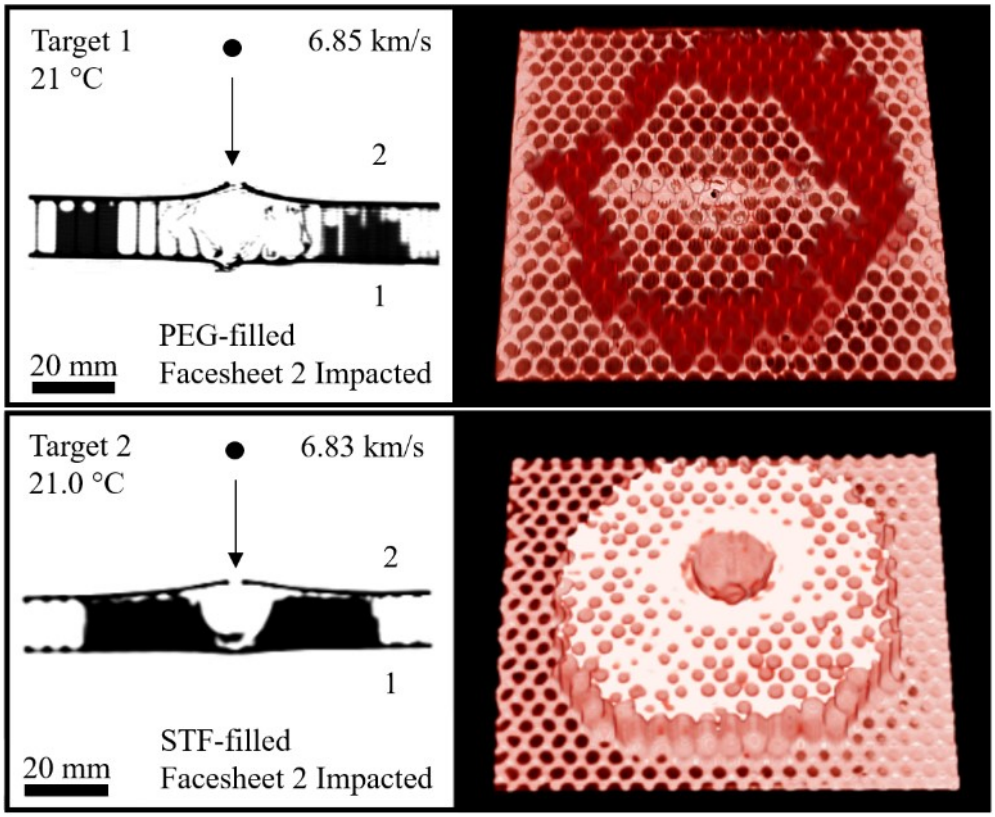

Figure 2.2 First comparison of PEG and STF imbibed panels

2D CT scans and 3D renderings of impacted PEG and STF-filled panels where Facesheet 2 was impacted, Top) PEG-filled core and impacted at $V_1 = 6.85$ km/s and at $T_1 \approx 21°C$ Bottom) STF-filled core and impacted at $V_1 = 6.83$ km/s and at $T_1 \approx 21°C$

There are two images shown for each panel. The left image is a single two-dimensional (2D) CT scan sectioned through the center of impact with a 1 and a 2 placed to indicate Facesheet 1 and Facesheet 2. Most of the PEG leaked out of the PEG-filled panel after the HVI making the individual honeycomb cell walls visible in the 2D CT images. The right image is a three-dimensional (3D) rendering of the entire specimen

impact-side up, where the impact-side facesheet is not shown in order to make visible the impact cavity within the liquid-filled honeycomb core. The honeycomb cell walls are much less visible in the 3D images due to the rendering; any solid mass observed in the cores in the 3D renderings is PEG or STF remaining in the honeycomb cells.

The back-side facesheet of the PEG-filled panel, the upper images in Figure 2.2, was perforated during the HVI. The 2D image shows that the projectile perforated the back-side facesheet but slightly off track of its original line of impact, and the entire exit hole is not visible due to the CT scans being taken at 0.5 mm intervals. This was the only instance of a back-side facesheet perforation in this study. The back-side facesheet of the STF-filled panel, the lower images in Figure 2.2, deformed slightly out-of-plane under the center of impact, but the back-side facesheet was not perforated. This demonstrates that the STF-filled honeycomb core provides greater impact mitigation than the PEG-filled core (the STF's liquid phase) under the same experimental conditions.

Other types of damage can be seen in Figure 2.2 aside from back-side facesheet perforation of the PEG-filled panel. For both the PEG-filled and STF-filled panels, the reduced bond strength of the impact-side facesheet, Facesheet 2, led to significant delamination of the facesheet from the core. The impact cavity in the core was formed by the lateral in-plane crushing of the honeycomb cells and fluid within them. The reduced bond strength of the impact-side facesheet caused the diameter of the impact cavity to be larger near the impact-side facesheet than near the back-side facesheet where the greater bond strength of the Facesheet 1 limited the delaminated area. This gave the impact cavity of both the PEG-filled and STF-filled panels an ogive-like shape. The number of damaged cells was greater in the PEG-filled panel than the STF-filled panel.

This is more evidence that the STF-filled panel can absorb the same amount of energy as the PEG-filled panel yet sustain less damage.

Figure 2.3 shows the CT scan imagery of a PEG-filled panel and a STF-filled panel impacted under the same conditions as the previous two panels in Figure 2.2, i.e., at room temperature ($T_1 \approx 21°C$) at the higher velocity ($V_1 \approx 6.8$ km/s). However, whereas Facesheet 2 was impacted for the previous two panels, Facesheet 1 was the impact-side facesheet for the panels in Figure 2.3. The only difference between the two panels in Figure 2.3 is one was PEG-filled and one was STF-filled.

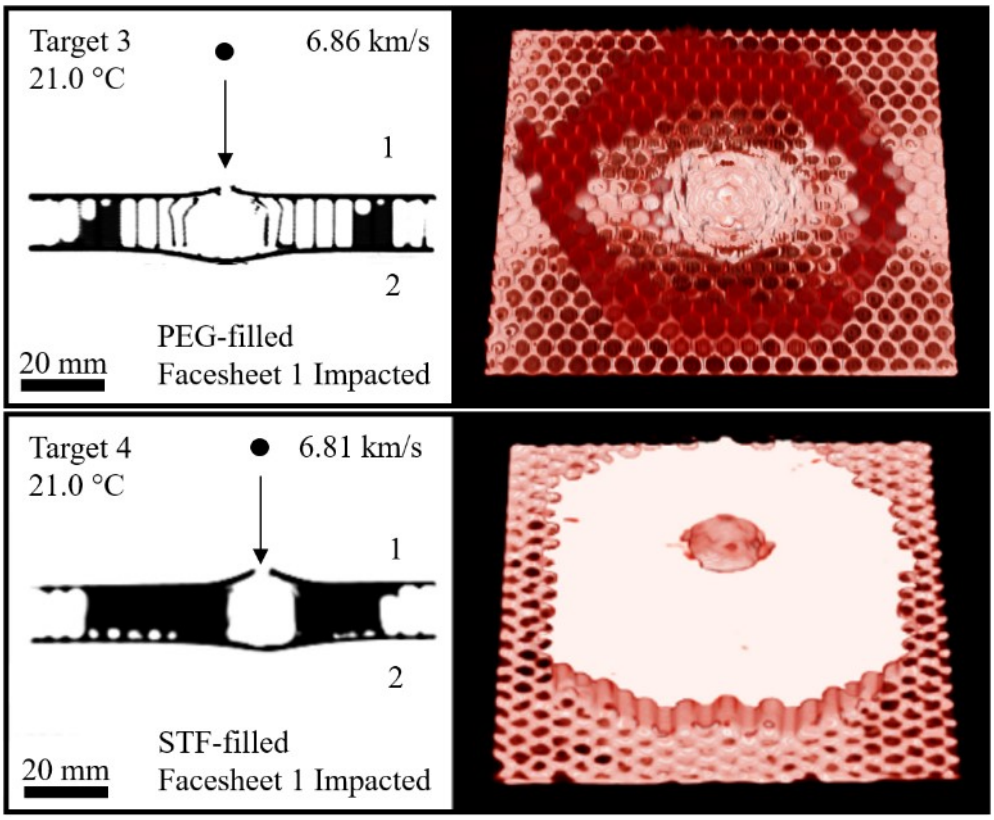

Figure 2.3 Second comparison of PEG and STF imbibed panels

2D CT scans and 3D renderings of impacted PEG and STF-filled panels where Facesheet 1 was impacted, Top) PEG-filled core and impacted at $V_1 = 6.86$ km/s and at $T_1 \approx 21°C$ Bottom) STF-filled core and impacted at $V_1 = 6.81$ km/s and at $T_1 \approx 21°C$

The back-side facesheet of the PEG-filled panel, the upper images of Figure 2.3, was not perforated as was the previous PEG-filled panel in Figure 2.2. This indicates that the choice of impact-side facesheet will affect the impact mitigation performance when panels are assembled as these were, i.e., Facesheet 1 is bonded to the honeycomb core, the honeycomb cells are filled, and then Facesheet 2 is bonded to the fluid filled core.

As in the previous two panels in Figure 2.2, there is a greater area of delamination of the core from Facesheet 2 than Facesheet 1 due to the of the reduced bond strength of Facesheet 2. The impact-side facesheet, Facesheet 1, with greater bond strength prevents a large area of the honeycomb core from delaminating. The impact cavity still expands outward as the honeycomb cells are crushed laterally in-plane. The core largely remains adhered to the impact-side facesheet and delaminates from the back-side facesheet. This caused the impact cavity of the panels in Figure 2.3 to be cylindrical in shape for both the PEG-filled and STF-filled panels. The impact cavity of the PEG-filled panel, the upper images of Figure 2.3, has a larger diameter than the STF-filled panel, the lower images of Figure 2.3, and a larger area of back-side facesheet delamination as well.

The energy absorption capability of the panels in Figures 2.2 and 2.3 is dependent on which fluid the core was filled with; the back-side facesheet of the PEG-filled panel was perforated while that of the STF-filled was not. The choice of impact-side and back-side facesheet matters as well. Consider the two PEG-filled panels impacted at the higher velocity, $V_1 \approx 6.8$ km/s, at room temperature, $T_1 \approx 21°C$. Facesheet 2 was impacted in Figure 2.2 resulting in perforation of the back-side facesheet, but the back-side facesheet of PEG-filled panel in Figure 2.3 where Facesheet 1 was impacted was not perforated.

Figure 2.4 shows the two STF-filled panels impacted at room temperature, $T_1 \approx$ 21°C, but at the lower impact velocity, $V_2 \approx 4.80$ km/s. The only difference between the panels in Figure 2.4 is whether Facesheet 1 or Facesheet 2 was impacted. Neither of the back-side facesheets of these STF-filled panels was perforated.

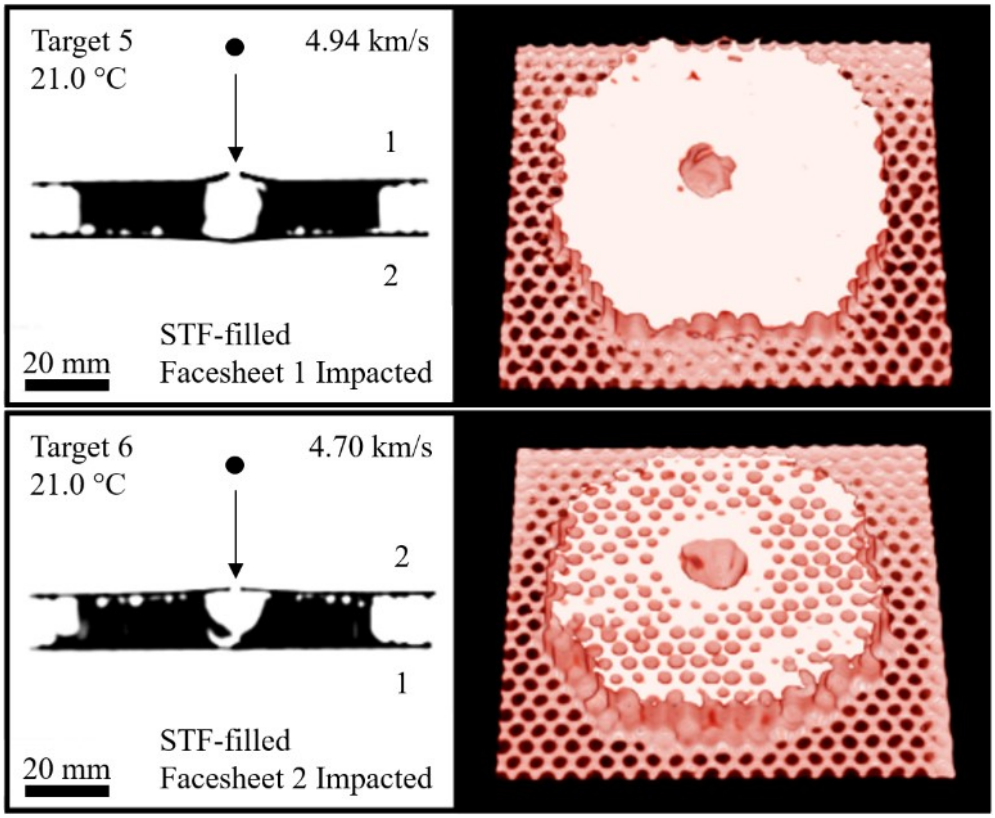

Figure 2.4 STF imbibed panels at room temperature, low velocity

2D CT scans and 3D renderings of impacted STF-filled panels, Top) Facesheet 1 impacted at $V_2 = 4.94$ km/s and at $T_1 \approx 21$°C, Bottom) Facesheet 2 impacted at $V_2 = 4.70$ km/s and at $T_1 \approx 21$°C

As seen in the previous STF-filled panels impacted at room temperature, the shape of the impact cavity in the fluid-filled honeycomb core and the deformation and delamination of the impact-side facesheet local to the impact depend on which facesheet

was impacted. The upper images of Figure 2.4 show that the impact cavity is cylindrical when Facesheet 1 was impacted. These upper images also show significant out-of-plane deformation of the impact-side facesheet. The lower images of Figure 2.4 where Facesheet 2 was impacted show that the impact cavity is ogive-like and that there is less out-of-plane deformation of the impact-side facesheet. The disparate areas of delamination of Facesheet 2 and Facesheet 1 seen in the higher impact velocity, $V_1 \approx$ 6.8 km/s, room temperature, $T_1 \approx 21°C$, of images of Figures 2.2 and 2.3 are not clearly evident in the panels of Figure 2.4 impacted at the lower impact velocity, $V_1 \approx 6.8$ km/s, at room temperature, $T_1 \approx 21°C$.

The remaining two figures cover the lower nominal temperature HVIs (≈ -80°C). Thermocouples were used to record the temperature of these panels during the HVIs; in each 3D rendering there is a hole in the upper right showing the thermocouple attachment point that is not associated with the HVI. Figure 2.5 shows two STF-filled panels impacted at the higher velocity, $V_2 \approx 6.8$ km/s, and lower temperature, $T_2 \approx -80°C$ where the STF was frozen solid. Neither of the back-side facesheets of the panels was perforated, and the only difference between the two is whether Facesheet 1 or Facesheet 2 was impacted. The upper images of Figure 2.5 show Facesheet 1 as the impact-side, and Facesheet 2 was impacted in the lower images. Unlike the STF-filled panels impacted at room temperature, the impact cavity of the two panels in Figure 2.5 have much the same roughly conical shape. Facesheet 1 for both panels shows more out-of-plane deformation rather than delamination local to the impact due to its greater bond strength. There is clear extensive delamination of Facesheet 2 for both panels with less

out-of-plane deformation than Facesheet 1. Visual inspection showed that this delamination of Facesheet 2 reached at least two lateral edges of the panels.

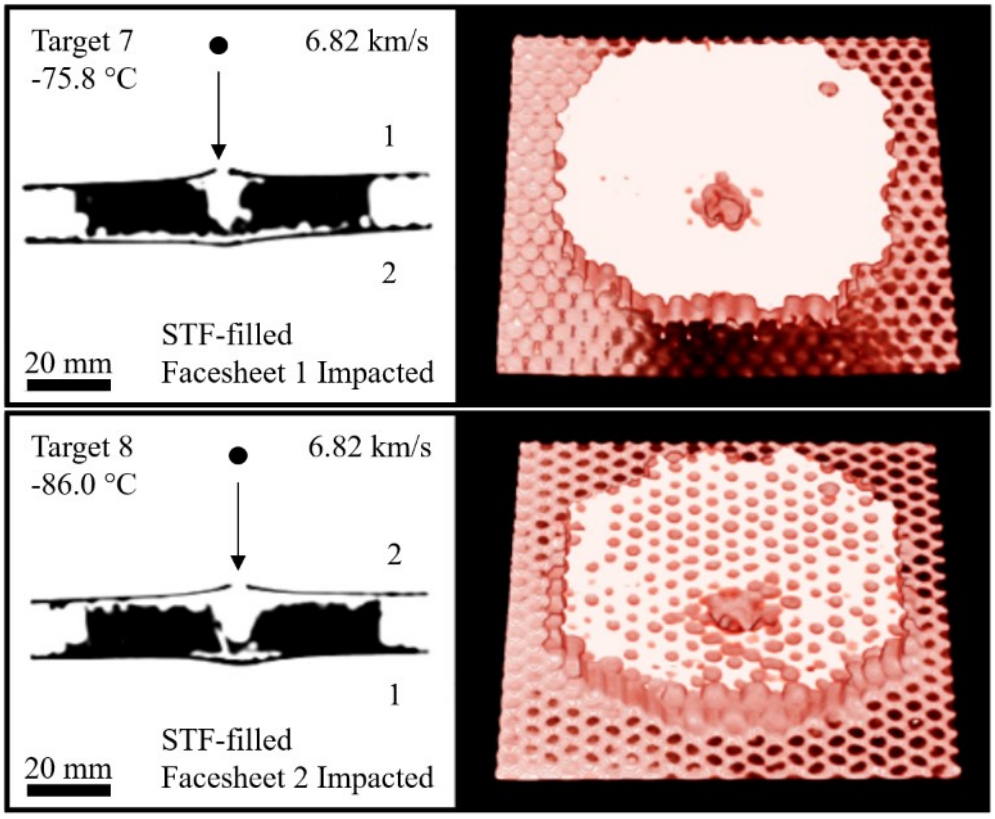

Figure 2.5 STF imbibed panels at low temperature, high velocity

2D CT scans and 3D renderings of impacted STF-filled panel, Top) Facesheet 1 impacted at V_2 = 6.82 km/s and at $T_2 \approx$ -75.8°C, Bottom) Facesheet 2 impacted at V_2 = 6.82 km/s and at $T_2 \approx$ -86.0°C

The two STF-filled panels impacted at the lower velocity, $V_2 \approx$ 4.8 km/s, and lower nominal temperature, $T_2 \approx$ -80°C, can be seen in Figure 2.6, and the only difference between them is whether Facesheet1 or Facesheet 2 was the impact-side facesheet. The back-side facesheets of these two panels were not perforated, and unlike the other panels in this study, the impact cavity inside the honeycomb core of neither of these panels

reached the back-side facesheet. Similar to the higher velocity, $V_2 \approx 6.8$ km/s, low nominal temperature, $T_2 \approx -80°C$, HVIs the shape and volume of the impact cavity in the panels of Figure 2.6 are roughly the same. Facesheet 2 was delaminated to at least two edges of both panels no matter which facesheet was impacted. There is out-of-plane deformation of the impact-side facesheet local to the impact. This is more pronounced in the upper images of Figure 2.6 where Facesheet 1 was impacted wherein the larger bond strength to the honeycomb core prevented a large area of delamination.

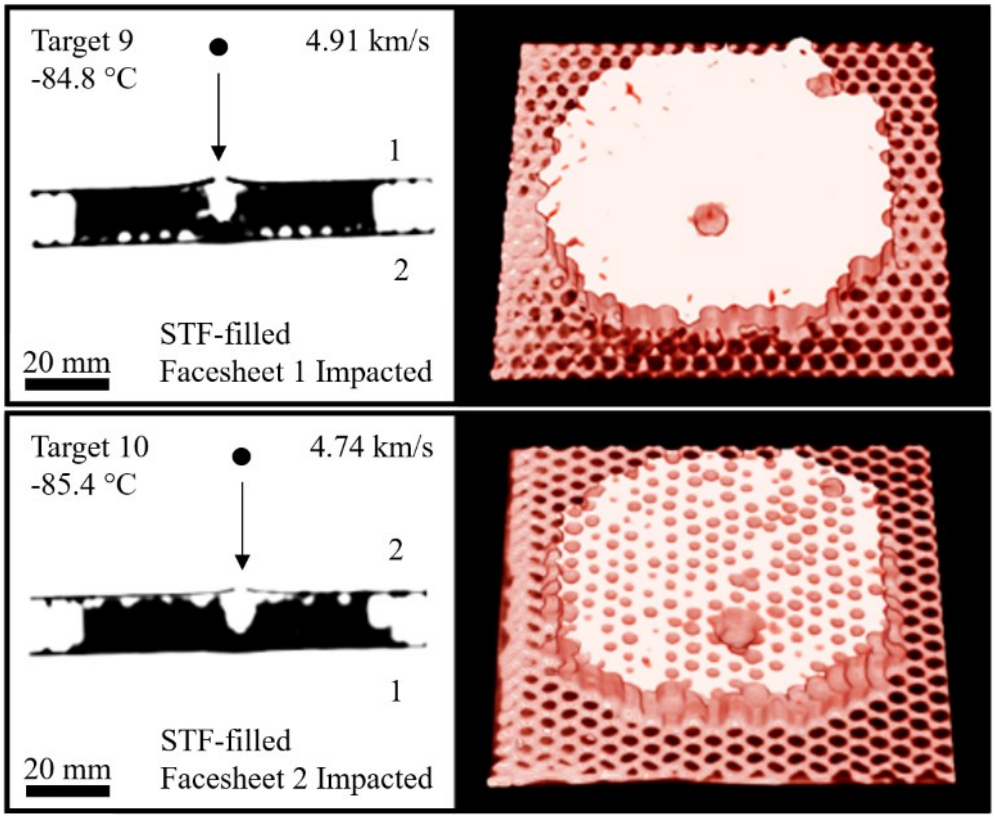

Figure 2.6 STF imbibed panels at low temperature, low velocity

2D CT scans and 3D renderings of impacted STF-filled panels, Top) Facesheet 1 impacted at $V_2 = 4.91$ km/s and at $T_2 \approx -84.8°C$, Bottom) Facesheet 2 impacted at $V_2 = 4.74$ km/s and at $T_2 \approx -85.4°C$

2.5 Conclusions

This study showed that under the same HVI test conditions, impact velocity and temperature, an aluminum sandwich panel with a honeycomb core imbibed with a STF provides better impact mitigation than one imbibed with PEG alone, the STF's liquid phase. The back-side facesheet of one PEG-filled panel was perforated while those of the STF-filled panels were not. The PEG-filled panels also sustained a greater volume of core damage in the form of laterally crushed honeycomb cells than the STF-filled panels.

The choice of the impact-side facesheet can affect the panel's impact mitigation capabilities when fluid filled panels are constructed using this method, i.e., Facesheet 1 is cured to the honeycomb core, the honeycomb is filled, and then Facesheet 2 is cured to the fluid filled core. When curing Facesheet 2, a portion of the adhesive flowed into the fluid partially starving the bond lines with the honeycomb core and resulting in a lower bond strength than the Facesheet 1 interface with the core. The PEG-filled panel whose back-side facesheet was perforated used Facesheet 2 as the impact-side facesheet. Under the same HVI conditions the back-side facesheet was not perforated when Facesheet 1 was the impact-side facesheet. Also, whether they were the impact side or not Facesheet 1 tended to show more out-of-plane deformation and Facesheet 2 more delamination.

Lowering the temperature of the HVI increased the STF-filled panels' impact mitigation effectiveness and greatly altered the extent and type of damage seen in the panels. At the lower temperature for the higher and lower impact velocity HVIs Facesheet 2 delaminated to at least two edges of each panels impacted while Facesheet 1 did not. For an actual MMOD shielding design suitable boundary conditions or stackup configuration would need to be applied to account for the delamination of Facesheet 2 to

the edge of the panel. The impact cavities resulting from all the lower temperature HVIs were of significantly less volume than the HVIs at room temperature at the corresponding impact velocities. Also, the low temp impacts at the same impact velocity tended to have same cavity shape no matter which facesheet was the impact side.

Future work would include using a STF-filled panel as a layer of a larger stack-up of MMOD shielding components as well as investigating HVIs of these panels at elevated temperature. An evaluation a STF-filled panel's multifunctional capabilities such as permeation barrier formation and radiation absorption could also be done.

CHAPTER III

EFFECT OF TEMPERATURE ON SHEAR THICKENING BEHAVIOR OF FUMED SILICA SUSPENSIONS

3.1 Introduction

Shear-thickening fluids (STFs) stand apart from other suspensions due to their remarkable shear rate dependent behavior. Beyond a critical applied shear rate, the viscosity of a STF increases rapidly, often by several orders of magnitude.[1,6,24,25] This rapid increase in viscosity has been exploited in novel applications such as improving the ballistic impact resistance of soft-body armor,[1,9] vibration damping of alpine skis,[10] as well as in spacecraft shielding concepts for mitigating highly energetic micrometeoroid/orbital debris (MMOD) impacts.[11]

The effectiveness of STFs in mitigating high-energetic particle impacts is presented in Figure 3.1. Here, two 10.16 cm x 10.16 cm aluminum facesheet sandwich composites with 1.27 cm thick aluminum honeycomb cores are shown after being impacted with a 1 mm diameter steel sphere (mass of 4 mg) traveling at 6.81 km/s (kinetic energy of 92.75 J). The central portion of the core of the specimen (target) shown in Figure 3.1 (top) was filled with polyethylene glycol of molecular weight of 200 g/mol (PEG 200), while the central portion of the specimen in Figure 3.1 (bottom) was filled with a STF consisting of 0.3 mass-fraction (MF) Aerosil 200 fumed-silica nanoparticles (A200 silica) in PEG 200. Note that there is both a larger volume of core

damage and rear facesheet penetration in the PEG 200-filled target versus the STF filled target. The STF-filled target sustained less core damage and no rear facesheet perforation. Since STFs show promise in mitigating high-energy impacts, these fluids might be useful as a supplementary component to MMOD shielding concepts. STFs suitable for these applications are required to have low solid volume-fractions for weight reduction and display shear-thickening responses over a wide temperature range, as the surface temperature of spacecraft structures can fluctuate over ±100°C.

STFs consist of a particulate phase dispersed in a suspending media. The interaction between the particles and the suspending media can be varied by selecting particles of different shapes, sizes, and surface chemistries to obtain a large variety of application-specific STFs. However, the mechanistic understanding of shear-thickening behavior required to design STFs for MMOD shielding applications from such a large parametric space is still incomplete. Further understanding of the effect of temperature on the shear-thickening behavior is limited. Previous studies of temperature variation were confined both in scope and temperature range.[22,26,27]

Several mechanisms have been associated with shear-thickening in the literature: i) an order-disorder transition,[28,29] wherein the alignment of suspended particles in ordered arrays at lower shear rates is disrupted by flow instabilities at higher shear rates leading to disordered structure, ii) dilatancy in high volume-fraction suspensions similar to that observed in granular solids[24] requiring the interstitial space between close packed particles to increase in order for particles to move past one other, and iii) the formation of transient particle aggregates defined as hydroclusters.[1,21,30,31] Additionally, frictional contact between rough particles has been shown to play an important role in certain

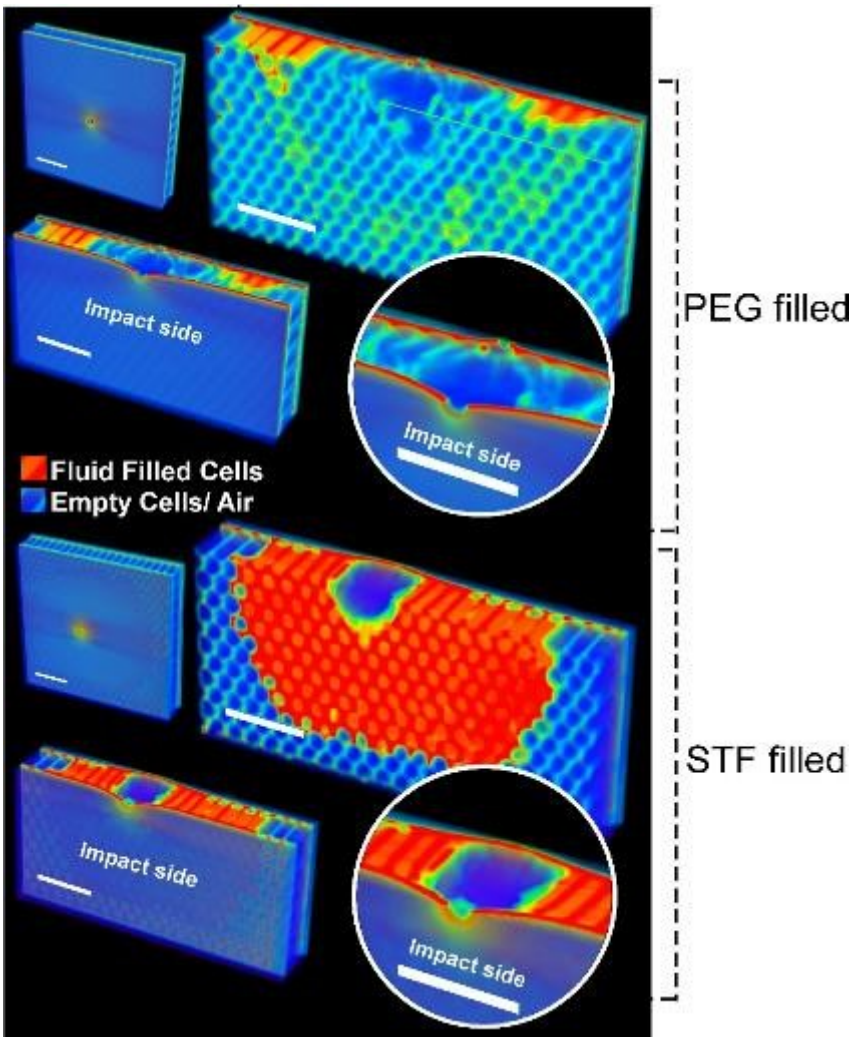

Figure 3.1 CT scans of impacted PEG and STF imbibed panels

Three-dimensional renderings of computed tomography scans of aluminum facesheet/ aluminum honeycomb core sandwich panels each impacted with a 1 mm diameter steel sphere (mass of 4 mg) at 6.81 km/s (kinetic energy of 92.75 J). Top) central portion of the core filled with polyethylene glycol with molecular weight of 200 g/mol (PEG 200). Bottom) central portion of the core filled with a shear-thickening fluid consisting of 0.3 mass-fraction Aerosil 200 fumed-silica nanoparticles in PEG 200 (Note: White scale bars are 20 mm in length.)

classes of suspensions.[32-37] Each mechanism involves particle movements, and the presence of one mechanism does not preclude or require the presence of another. The shear-thickening response of a STF is dependent on the particular characteristics of that

system. As the particles move, the interactions between the particles and between particles and suspending media change. These changes will be a function of shear rate and temperature. Several interactions are of interest, for example, van der Waals, electrostatic, steric, frictional, hydrodynamic, and Brownian. These interactions contribute to a complex balance of forces that can lead to transient cluster formations and/or frictional contacts. The formation of these so called hydroclusters corresponds to a marked increase of viscosity. Evidence of hydrocluster formation has been observed in small angle neutron scattering (SANS),[31] and the present study also indicates that hydrodynamics play an important role in shear-thickening behavior.

At low applied shear rates the viscosity of many STFs will initially decrease (i.e., shear thinning behavior), as the at-rest microstructure is disrupted.[1] Here, repulsive forces between the particles play an important role. For instance, the presence of particle surface charge can result in electrostatic repulsive forces that could prevent two particles from coming into close proximity, decreasing the likelihood of shear-thickening. Shearing deformation of the suspending media induces hydrodynamic drag forces on the particles. The hydrodynamic drag force, which is proportional to the applied shear rate, causes the particles to translate and rotate.[38] As the shear- rate increases, so too does the hydrodynamic drag force, leading to more particle movement and an increased likelihood that particles will approach one another.

At a critical shear rate the sum of the repulsive forces acting on the particles (electrostatic and steric repulsion, Brownian effects, etc.) are overcome by the sum of the forces acting to bring the particles into close proximity. According to lubrication hydrodynamics, when two particles approach one another, the suspending media between

them must be displaced, and the force required to displace this suspending media is a function of the inverse of the distance between particle surfaces.[25,39] This leads to the theoretical lubrication singularity at zero interparticle distance preventing particle surface-to-surface contact.[25,39] Thus, for particles to come into close proximity at and above the critical shear rate the hydrodynamic forces must be very high to overcome lubrication force and any other repulsive forces.[1] However, the distance between the particles is dictated by the repulsive forces acting between them. Once the interparticular distance between two particles is small enough, the two particles will theoretically enter into closed orbits wherein the two particles cannot be separated unless a separating force is acting upon them equal in magnitude to the force required to bring them together.[1,25] These hydrodynamic lubrication forces cause the formation of hydroclusters.[1,25] As the name suggests, hydroclusters are transient structures of coalesced particles.[25] Simulations have indicated that the number and size of hydroclusters increases with increasing shear rate.[1,21,30,] Significant energy is dissipated to bring the particles into close proximity, and as a result, the characteristic viscosity increase of STFs takes place.[1]

However, Zhao and Davis showed that the lubrication singularity as well as closed orbits can be avoided for two spheres approaching in low Reynolds number flow if their surfaces are roughened.[40] This can allow particle surface-to-surface contact and, hence, the development of frictional contact forces. Such frictional contact forces have been shown to play an essential role in producing strong shear-thickening in concentrated suspensions both in simulations and experiments.[32-37] Mari et al. notes that while hydrodynamic lubrication forces are influential to the behavior of lower concentration suspensions, frictional contact forces play a key role in the behavior of highly

concentrated suspensions.[32] Interestingly, Heussinger reported shear-thickening and cluster formation in simulations of non-Brownian frictional particles where hydrodynamic lubrication forces were intentionally neglected.[34] Furthermore, using confocal microscopy Lootens et al. observed a formation of ordered (jammed) structure in high concentration suspensions of roughened particles.[36] Clearly, shear-thickening is an intricate phenomenon that can be caused by or related to a variety of physical principles that would depend on the characteristics of each particular system.

The mechanisms leading to shear-thickening behavior are best understood for STFs based on spherical suspended particles. Hydrocluster formation involving the irregularly shaped fractal-like fumed-silica nanoparticles used in this study likely involve similar controlling principles, but the effects of shape, aspect ratio, size, volume-fraction of the suspended particles, and alignment of the particles during shear are very complex. The inherent roughness of fumed-silica particles due to their branched aggregate nature also raises interesting questions concerning friction as well as possible interlocking of particle branches, and this will be postulated later.

Most recent literature on STFs has considered spherical particles which undergo dramatic shear-thickening only at very high particle volume-fractions.[24] However, STFs employing irregularly shaped particles, such as fumed-silica nanoparticles, can exhibit shear-thickening intensities similar to suspensions based on spherical particles but at much lower volume-fractions.[41-45] This is beneficial because reducing the suspended particle volume fraction could lead to significant weight savings for many STF applications. In addition, the shear-thickening response can be tailored by modifying the surface of the fumed-silica particles with various functional groups. Hence, changes in

the chemical functionality of the particle surfaces can be used to tune the particle-liquid interactions when paired with an appropriate choice of suspending media.[42]

Since the motivation of our research is designing a relatively low density STF that could be used as a component in shielding to protect spacecraft from MMOD impacts, fumed-silica nanoparticles were chosen as the dispersed phase. We report here the shear-thickening responses and the effect of temperature on these responses for suspensions of fumed-silica nanoparticles where the mass-fraction and surface chemistry of the fumed-silica as well as the molecular weight and architecture of the suspending media were varied. Present theoretical understanding of shear-thickening based on hard-sphere suspensions cannot be applied to fumed-silica suspensions directly, but an attempt has been made here to explore the complex underlying contributions of the various factors leading to shear-thickening. Experiments were conducted over temperature ranges spanning approximately 100°C. The critical shear rate marking the onset of shear-thickening was found to be inversely proportional to the viscosity of the pure suspending media over the temperature range investigated. This shear-thickening was attributed to hydrocluster formation caused by the balance of hydrodynamic, steric, frictional, and thermal forces that govern particle interactions.

3.2 Materials and Methods

Two types of fumed-silica nanoparticles and three low molecular weight oligomeric glycols (suspending media) were selected to generate the four STFs produced for this study. These suspending media included hydroxyl-terminated polyethylene glycol of molecular weight of 200 g/mol (PEG 200) and of molecular weight of 400 g/mol (PEG 400), and a three-armed glycerol polypropylene oxide having a

molecular weight of 700 g/mol (PPG 700). Two types of fumed-silica nanoparticles were selected: Aerosil 200 (A200 silica) and Aerosil R812 (R812 silica) (Evonik Industries).

A200 and R812 fumed-silica nanoparticles consist of approximately spherical SiO_2 primary particles fused together during a flame hydrolysis manufacturing process to form irregularly shaped branched aggregates.[46] The A200 and R812 particles have different surface functional groups (discussed later), so they will interact differently with the suspending media, and the corresponding temperature dependent shear-thickening behavior will be different. Representative transmission electron microscopy (TEM) images of A200 and R812 silica are shown in Figure 3.2A and 3.2B, respectively. TEM images of fumed-silica particles were captured using a JEOL 2100 200 kV microscope. Dilute solutions of fumed-silica particles in ethanol were deposited on carbon coated copper grids. Excess ethanol was dried before TEM experiments. Based on the

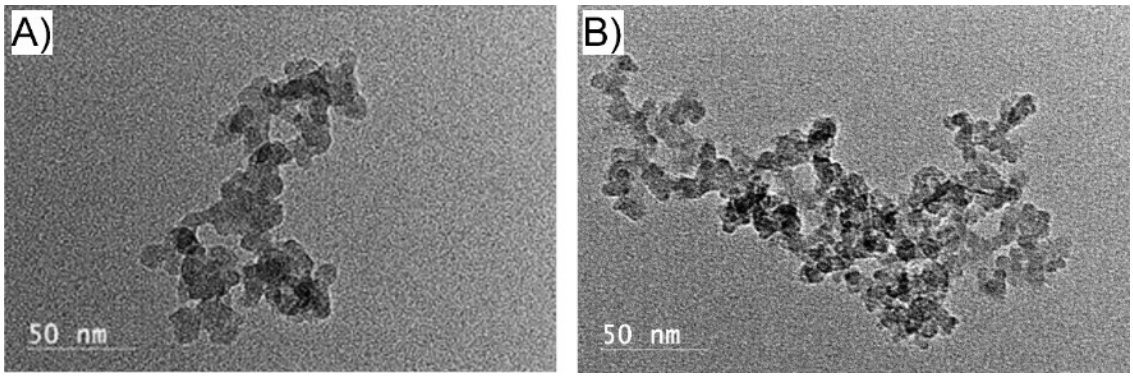

Figure 3.2 TEM images of fumed silica

Representative transmission electron micrographs of A) Aerosil 200 fumed-silica nanoparticles, displaying the aggregates formed of ~12 nm diameter spherical SiO_2 primary particles fused and B) Aerosil R812 fumed-silica nanoparticle aggregate with ~7 nm diameter spherical SiO_2 primary particles (Note: Image B very likely consists of 2 to 3 agglomerated nanoparticles)

literature[46-48] and TEM data, the A200 primary particle size is ~12 nm and the characteristic length of the aggregates is ~100-200 nm. The A200 silica particles have a specific surface area of ~200 m^2/g.[46-48] The R812 silica particles have a ~260 m^2/g specific surface area and the primary particle size is ~7 nm.[46-48] TEM images indicated that R812 particles have a similar characteristic length as A200 particles.

The fumed-silica particles were dried in an oven at 105°C for at least 24 h and then dispersed in PEG or PPG using a Silverson L4RT-A high shear mixer. As shown in Table 3.1, three of the four STFs produced for this study were PEG suspensions: i) 0.15 mass-fraction (MF) A200 silica in PEG 200, ii) 0.225 MF A200 silica in PEG 200, iii) 0.15 MF A200 silica in PEG 400 and iv) STF 0.15 MF R812 silica in PPG 700. All STFs were degassed in a vacuum oven for approximately 1 h to remove air incorporated into these suspensions during the high shear mixing.

Table 3.1 Shear thickening composition and temperature ranges

Silica			Suspending Fluid	Temperature Range	Melting Point of Suspending Media
Type Used	Mass-fraction	Volume-fraction			
A200	0.150	0.0696	PEG 200	-60°C – 40°C	-65°C
A200	0.225	0.1096	PEG 200	-50°C – 40°C	-65°C
A200	0.150	0.0699	PEG 400	10°C – 80°C	6°C
R812	0.150	0.0641	PPG 700	-40°C – 40°C	-32°C

Steady-shear rheological experiments on the STFs were conducted using a TA Instruments Discovery Hybrid 2 rheometer with 25 mm diameter parallel plate fixtures. The environmental chamber of the rheometer was utilized to conduct experiments over a

maximum accessible temperature range for each fluid as shown in Table 1. The lowest experimental temperature employed was either i) just above the melting point of the corresponding suspending media, or ii) limited by the maximum torque limit of the instrument as decreasing temperatures caused higher viscosities and rising torque values. The maximum temperature investigated was limited by either i) the lower torque limit of the instrument or ii) loss of low-viscosity samples from the rheometer fixture before achieving the critical shear rate. Additional experiments over a limited temperature range were also performed using a Peltier device, which allowed imaging of the free-surface of the sample during shearing. All experiments were repeated at least three times.

The PEG and PPG molecular structures are shown in Figure 3.3. The number of repeat units in Figure 3.2 for PEG 200 and PEG 400 are $n \approx 4$ and $n \approx 8$, respectively (Figure 3.3A). The sum of the repeat units x, y, and z for PPG 700 is ≈ 10 (Figure 3.3B).

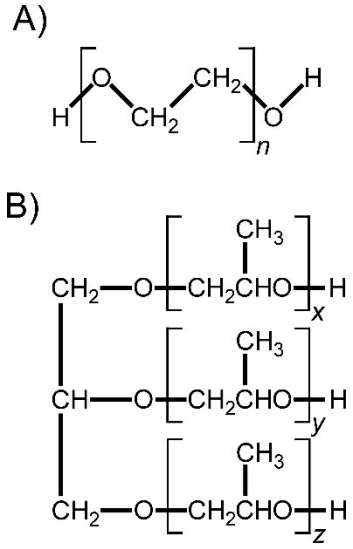

Figure 3.3 Polymer chemical structures

Chemical structures of A) polyethylene glycol (PEG 200 and 400) and B) glycerol polypropylene oxide (PPG 700)

The branched (three-armed star) architecture of PPG 700 results in three terminal hydroxyl groups per molecule as opposed to two for the linear PEG 200 and PEG 400 molecules. The ratio of terminal hydroxyl groups to internal oxygens (ether linkage) for PEG 200, PEG 400 and PPG 700 are approximately 3.5:2, 7.5:2, and 10.5:3. The melting points of the suspending media are -65°C, 6°C, and -32°C, respectively, as provided by the manufacturer.

3.3 Results and Discussion

3.3.1 Shear Thickening Behavior

Figure 3.4A displays a representative plot of the average viscosity versus shear rate on a log-log scale for 0.15 MF A200 silica in PEG 200 measured at 20°C. Initially a shear-thinning behavior is observed for shear rates of approximately 1 s^{-1} to 100 s^{-1} wherein viscosity decreases with increasing shear rate. However, beyond a critical shear rate of approximately 100 s^{-1} the viscosity increases (i.e., shear-thickens) over shear rates of approximately 100 s^{-1} to 400 s^{-1}. This demonstrates the characteristic attribute of STFs that differentiates them from other suspensions: their viscosity at the higher shear-rates can be larger in magnitude than their viscosity at lower shear-rates.

In addition to changes in an STF's viscosity, changes in the samples free surface can also occur with increasing shear-rate. Images of the 0.15 MF A200 silica in PEG 200 sample's free surface taken at three important conditions of a rheological experiment are shown as insets in Figure 3.4A. These images were captured (from left to right) i) during shear thinning, ii) near the critical shear-rate, and iii) during advanced shear-thickening (corresponding data points are shown by arrows). Interestingly, the free surface of the sample displayed no visible change at the critical shear-rate. However, as the shear-

thickening developed, instabilities formed on the free surface (image corresponding to the highest shear-rate in Figure 3.4A). These instabilities eventually caused a portion of the sample to be ejected, limiting the magnitude of the viscosity increase that could be studied. The loss of sample reduced the torque required to maintain the shear-rate, resulting in a decrease in apparent viscosity not representative of the true STF viscosity. Surface-instabilities can be caused by many factors.[49] Here, they are thought to be related to the hydrocluster formation mechanism occurring during the shear-thickening process. The critical shear-rate and associated critical shear stress marking the onset of

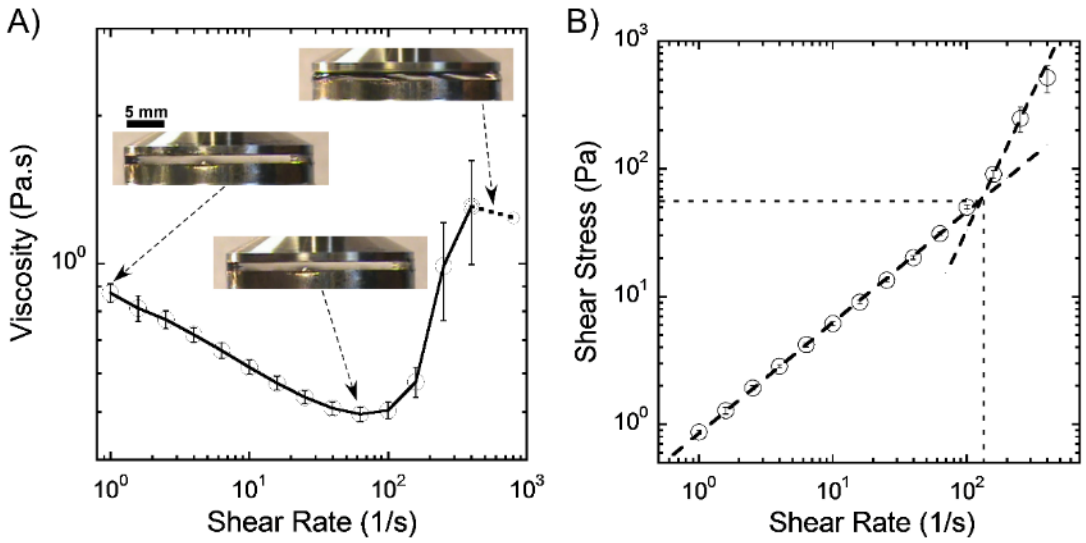

Figure 3.4 Shear thickening behavior

A) Viscosity versus shear rate for 0.15 mass-fraction Aerosil 200 fumed-silica in polyethylene glycol with molecular weight of 200 g/mol at 20°C with images of the sample taken at three key conditions during a steady-shear experiment. The line connecting the points is not a model fit and is provided for visual guidance only. B) Determination of the critical shear rate and associated shear stress based on the change in slope of the shear stress versus shear rate curve. (Note: All error bars represent one standard deviation.)

shear-thickening behavior were calculated as done by Boersma et al.[26] by determining the point at which the slope changes on the shear stress versus shear rate curve plotted on a log-log scale as shown in Figure 3.4B.

3.3.2 Experimental Results

Steady-shear rheological data (i.e., viscosity versus shear rate plotted on log-log scales) for the four STFs considered in this study over the temperature ranges in Table 1 are displayed in Figure 3.5. Generally, these plots followed the same trends as those discussed for the viscosity versus shear rate curve in Figure 3.4A. Consider Figure 3.5A, which displays the viscosity versus shear rate curves for 0.15 MF A200 in PEG 200 over a temperature range of -40°C to 40°C. The curve in Figure 3.4A is actually the curve marked by solid orange triangles in Figure 3.5A. Viscosity versus shear rate curves for all experimental temperatures follow the same trends as discussed for Figure 3.4A. For example, the viscosity of the -40°C curve in Figure 3.5A (marked by solid blue triangles) decreases over shear rates of approximately 0.01 s^{-1} to 0.06 s^{-1} (i.e., shear thinning) before the viscosity rises markedly (i.e., shear thickening) after a critical shear rate of approximately 0.1 s^{-1}.

Reducing the temperature of an experiment was seen to have four effects on the viscosity versus shear rate curve. First i), lowering the temperature of an oligomeric liquid generally increases its viscosity, and this is evident in Figure 3.5A where the first few data points of each temperature curve indicate higher initial viscosities as the temperature decreases. Second ii), lowering the temperature also decreased the critical shear rate; lowering the temperature from 20°C to -40°C reduced the critical shear rate

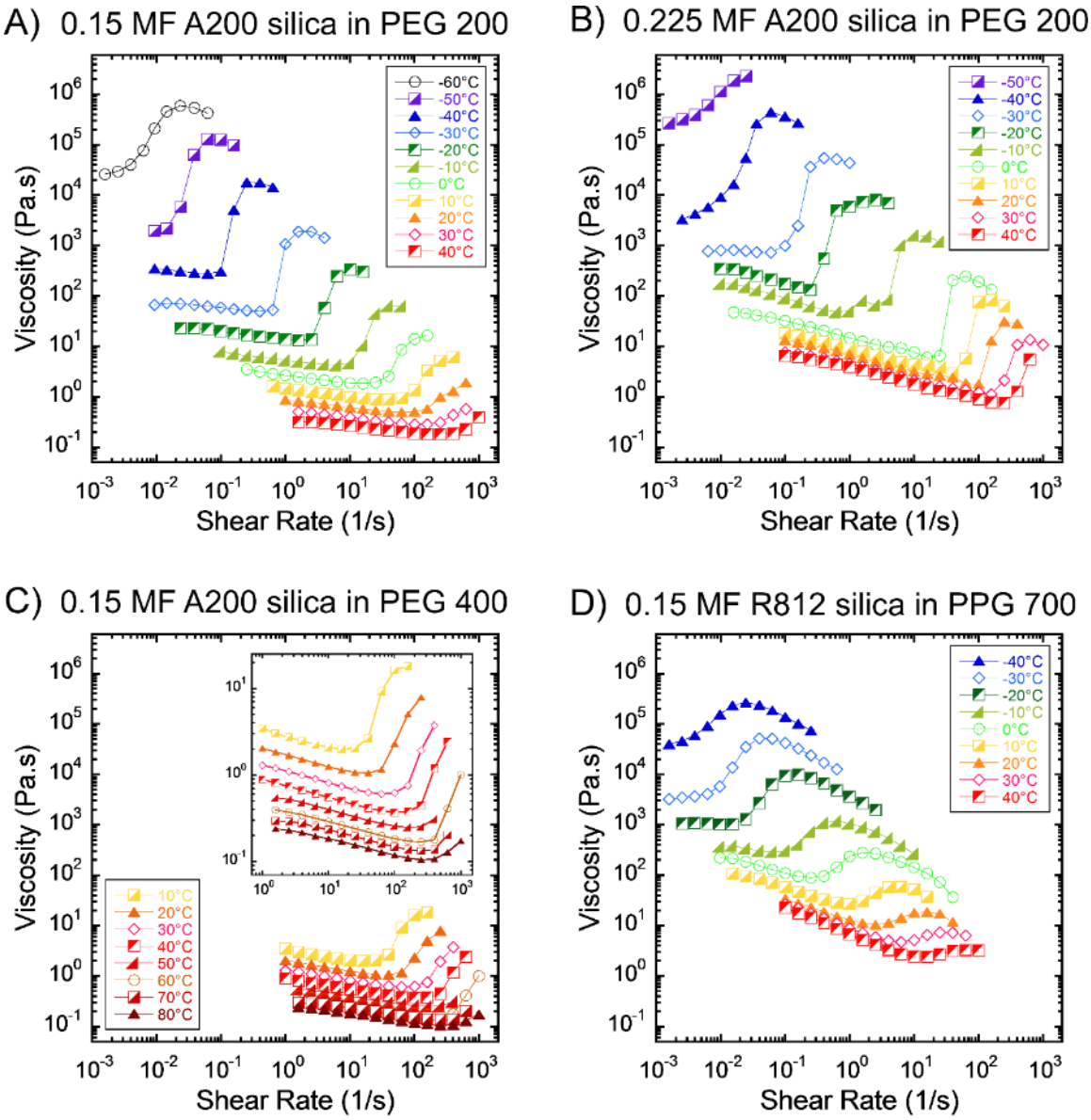

Figure 3.5 Rheological characterizations of the STFs

Steady-shear experimental results as a function of temperature for: A) 0.15 mass-fraction (MF) Aerosil 200 fumed-silica (A200 silica) in polyethylene glycol of molecular weight of 200 g/mol (PEG 200), B) 0.225 MF A200 silica in PEG 200, C) 0.15 MF A200 silica in polyethylene glycol of molecular weight of 400 g/mol (PEG 400) (note: inset shows the viscosity axis expanded), and D) 0.15 MF trimethylsilated Aerosil R812 fumed-silica in glycerol propylene oxide with molecular weight of 700 g/mol

from approximately 100 s^{-1} to 0.1 s^{-1}. Third iii), as the temperature decreases the

viscosity increases more rapidly following the critical shear rate (i.e., the steepness of the

shear thickening portion of each curve). Lastly, the overall increase in the magnitude of the viscosity after the critical shear rate increases as the temperature decreases. For example, the viscosity at the critical shear rate for -40°C (Figure 3.5A) is approximately 300 Pa.s and rises to a maximum value of around 20,000 Pa.s (nearly two orders of magnitude) while the increase of viscosity is approximately 0.5 Pa.s to around 2 Pa.s (less than one order of magnitude) at 20°C.

The effect of increasing the mass-fraction of the suspended particles can be seen by comparing Figures 3.5A and 3.5B. The suspending media was the same for each of these plots (PEG 200), but the mass-fraction of A200 silica was increased from 0.15 MF in Figure 3.5A to 0.225 MF in Figure 3.5B. Increasing the silica MF from 0.15 to 0.225 in PEG 200 increased the viscosity of corresponding STFs. For example, the viscosity at a shear rate of 10 s^{-1} at 20°C (curves marked by solid orange triangles), for 0.15 MF (Figure 3.5A) and 0.225 MF (Figure 53.B) are approximately 0.9 Pa.s and 7 Pa.s, respectively, nearly an order of magnitude. Increasing the mass-fraction also slightly reduced the critical shear rates. For instance, the critical shear rate at 40°C (curves marked by half-filled red squares) was approximately 500 s^{-1} for the 0.15 MF sample (Figure 3.5A) while that of the 0.225 MF sample (Figure 3.5B) was approximately 200 s^{-1}. Additionally, the viscosity increased more rapidly following the critical shear rate (i.e., the steepness of the shear thickening portion of the curve) when the MF was increased, which is evident when comparing the 0°C curves, marked by hollow green circles in Figures 3.5A and 3.5B.

Figure 3.5C shows the viscosity versus shear rate curves for the 0.15 MF A200 silica in PEG 400 over a temperature range of 10°C to 80°C. A smaller temperature

range could be accurately investigated for the PEG 400 suspension (Figure 3.5C) as some portions of the samples were ejected from the rheometer geometry early for experimental temperatures above 50°C.

Increasing the suspending media molecular weight from 200 g/mol to 400 g/mol had similar results on the shear rate and temperature dependent behavior as did increasing the suspended particle mass-fraction from 0.15 MF to 0.225 MF. However, the rheological behavior of the 0.15 MF A200 silica in PEG 400 STF was less shear rate and temperature dependent than the 0.15 MF A200 silica in PEG 200 and 0.225 MF A200 silica in PEG 200 STFs. Recall that PEG 400 has an inherently larger viscosity than PEG 200. Comparing the viscosity at a shear rate of 10 s^{-1} at 20°C, for the PEG 200 based STF in Figure 3.5A and the PEG 400 based STF in Figure 3.5C, the viscosity increased from approximately 0.9 Pa.s to 2 Pa.s due to the higher molecular weight. The critical shear rate decreased slightly for the higher molecular weight sample. For example, the critical shear rate at 40°C was approximately 500 s^{-1} for the PEG 200 sample (Figure 3.5A) while that of the PEG 400 sample (Figure 3.5C) was approximately 100 s^{-1}. Comparing the 30°C curves of Figures 3.5A and 3.5C, the viscosity increased more rapidly following the critical shear rate (i.e., the steepness of the shear thickening portion of the curve) when the molecular weight of the suspending media was increased.

For the hydrophilic suspended particles (A200 silica) and polar suspending media (PEG 200 or PEG 400) hydrogen bonding is significant (to be discussed later). However, Figure 3.5D shows the results of experiments for a STF of 0.15 MF R812 silica in PPG 700 where the hydrogen bonding interactions are much reduced due to the hydrophobic nature of R812 silica leading to differences in the shear thickening behavior

discussed below including a second shear thinning region when compared with the PEG-based STFs in Figures 3.5A, 3.5B, and 3.5C.

Note that some trends are similar to the PEG-based STFs. The first few data point of each curve show that the viscosity of the STF increases as the temperature falls. Lowering the temperature also decreases the critical shear rate. The viscosity increases more rapidly following the critical shear rate (i.e., the steepness of the shear thickening portion of each curve) at lower temperatures. Although, it is evident from comparing the -10°C curves marked by green right triangles from Figures 3.5D and 3.5A that the viscosity generally increases less rapidly for the 0.15 MF R812 silica in PPG 700 STF than for a PEG-based STF. Decreasing the temperature leads to larger overall increases in the magnitude of the viscosity after the critical shear rate, but not as large an increase in magnitude as the PEG-based STFs, which can be seen by comparing again the -10°C curves in Figures 3.5D and 3.5A.

One interesting behavior of the 0.15 MF R812 in PPG 700 STF is that the shear-thinning before the critical shear rate is more pronounced when the temperature is increased, i.e., the shear-thinning region is steeper with increased temperature. This can be seen by comparing the results for -10°C and 40°C in Figure 3.5D. Additionally, a pronounced shear thinning region follows the shear thickening region of most of the curves in Figure 3.5D. Following the concept of shear thinning, this must mean that after the shear thickening regime the particles are realigning themselves to more easily move past each other. The surface of the 0.15 MF R812 in PPG 700 STF remained stable over a larger range of shear rates beyond the critical shear rate.

These results indicate the slope of the viscosity versus shear rate curve changes with the sample composition. Such changes can be qualitatively described as either continuous or discontinuous shear-thickening processes.[24] Continuous shear-thickening represents a gradual increase of viscosity, whereas, a very rapid increase of viscosity is described as discontinuous shear-thickening. The difference between these behaviors can be clearly seen on a viscosity versus shear stress curve by considering the slope of the linear region of the shear-thickening portion of the curve (i.e., portion of curve where the viscosity increases following the shear thinning region). In general, for discontinuous shear thickening, the slope of the viscosity versus shear stress curve will exceed unity in the shear thickening regime.[24] Figure 3.6 shows the viscosity versus shear stress curve for each of the four STFs at 20°C along with a dashed line with a slope of unity. It is clear that all four STFs exhibit continuous shear-thickening. However, consider the results for both 0.15 MF and 0.225 MF A200 in PEG 200 (marked by the green right triangles and blue half solid squares, respectively). As the silica MF is increased, the shear-thickening slope approaches a value of one. Thus, the shear thickening approaches a discontinuous behavior. At some silica MF greater than 0.225 A200 in PEG 200, the STF would be expected to display discontinuous shear-thickening behavior. Note that the 0.15 MF R812 silica in PPG 700 STF marked by solid black circles in Figure 3.6, where the hydrogen bonding between the suspended silica particles and the suspending media is reduced when compared with the A200 silica based STFs, displays significantly more continuous behavior than the three PEG-based STFs.

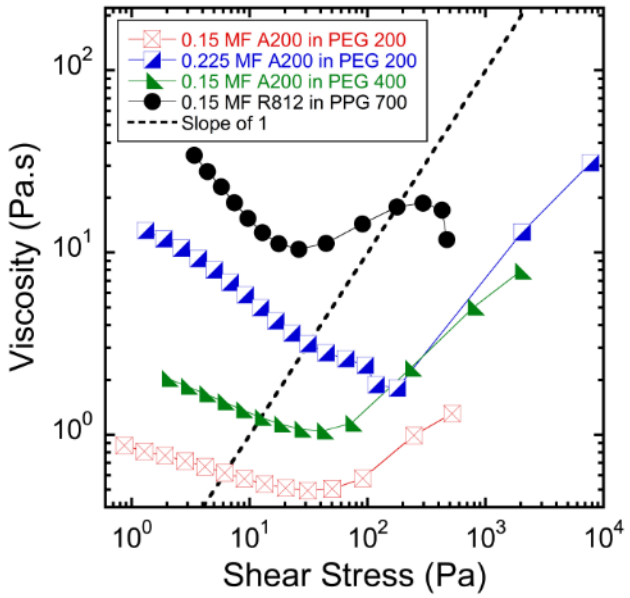

Figure 3.6 Continuous and discontinuous shear thickening

Viscosity versus shear stress for four different STFs at 20°C along with an arbitrarily placed dashed line with a slope of one. Slope values of the shear-thickening portions of the curves greater than zero indicate shear thickening, and slope values equal to or greater than one are regarded as discontinuous shear thickening.

3.3.3 Surface Chemistry and Solvation Layer

The different shear-thickening behaviors discussed previously depend on the suspended particles' morphologies and surface chemistry, which affected the degree to which the suspended particles formed hydrogen bonds with the suspending media, resulting in either more hydrogen bonding (A200 silica in PEG 200/400) or less hydrogen bonding (R812 silica in PPG 700). The large silica surface area enables surface functional group interactions with the suspending media to greatly impact how these particles respond to hydrodynamic forces, and, hence, their hydrocluster formation.[46,48] The main functional groups present on fumed-silica (Figure 3.7A-C) include isolated silanol groups, bridged silanol groups, and siloxane oxygens.[48] The isolated and bridged

silanol group surface densities for A200 silica are ~1.15 /nm^2 and ~1.35 /nm^2, respectively.[47,48] These hydroxyl groups acidify A200 silica to pH values of 3.7 to 4.7 and render A200 silica hydrophilic. When A200 silica is dispersed in the PEGs used in this study, hydrogen bonds readily form between the silanol groups on the A200 silica surfaces and PEG.

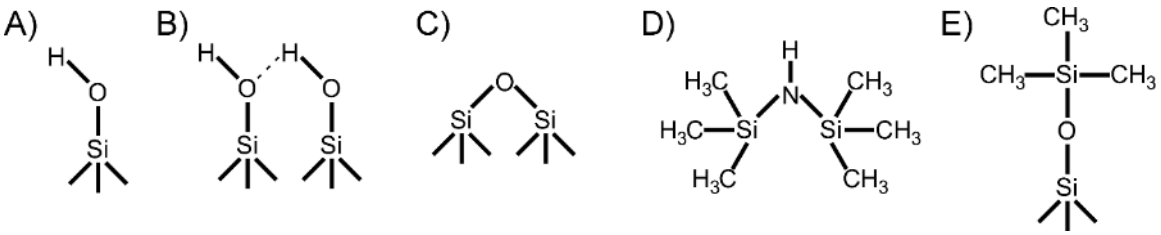

Figure 3.7 Surface functional groups

Chemical structures of A) isolated silanol group, B) bridged silanol group, C) siloxane group, D) hexamethyldisilazane, and E) trimethylsilyl surface groups.

In contrast to A200 silica, R812 silica is hydrophobic. R812 silica is made from Aerosil 300 (A300 silica) (Evonik Industries) which has a specific surface area of ~300 m^2/g. A300 silica is post-treated with hexamethyldisilazane (Figure 3.7D), which results in conversion of the isolated silanol groups of A300 silica to trimethylsilyl groups (Figure 3.7E).[46,47] This marginally reduced the surface area of R812 to ~260 m^2/g. The bridged silanol groups on A300 silica are partially retained on the surface of R812 silica with a surface density of ~0.44 /nm^2 after treating with hexamethyldisilazane.[48]

In bulk liquid PEG and PPG, hydrogen bonding occurs between hydroxyl-terminated end groups as well as between hydroxyl end groups and internal ether groups. However, the propensity of hydrogen bonding is higher near the fumed-silica surfaces (particularly, A200), which have a large number of silanol groups. Silanol groups are

more acidic than the terminal hydroxyls of PEG and better hydrogen bond donors. Figure 3.8 shows several of these hydrogen bonding possibilities between the suspending media and the silanol groups present on the fumed-silica surfaces. Note that all hydrogen bonds are in dynamic equilibrium, rapidly forming and breaking. Multiple hydrogen bonds may exist between individual molecules of PEG (or PPG) and silica, reducing the rate of exchange of these suspending fluid molecules at the surface with bulk fluid. All surface hydrogen bonds between silica and a suspending media molecule must have broken for that molecule to diffuse away from the surface, which is very unlikely. Hydrogen bonding results in development of a solvation layer near the surface, where the

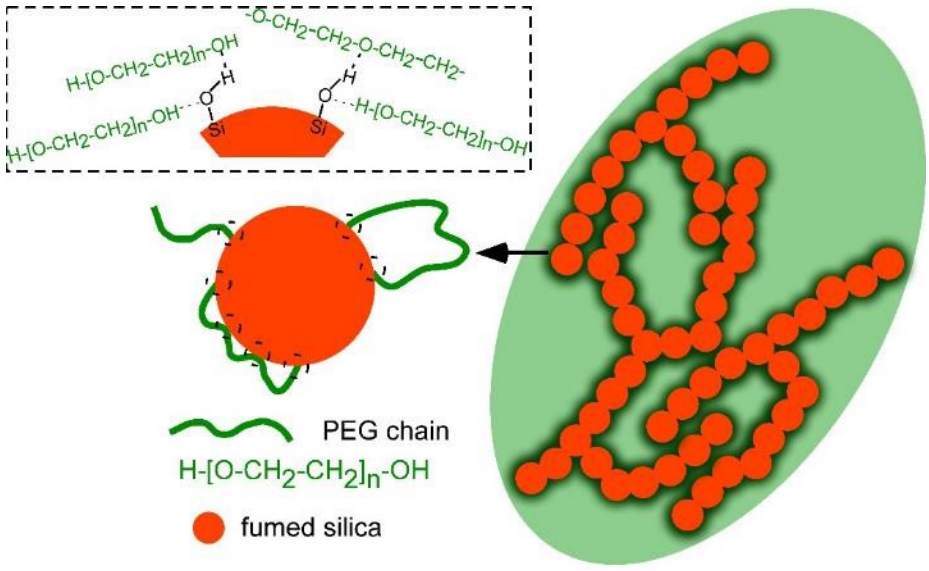

Figure 3.8 Hydrocluster formation

Schematic representation of proposed hydrocluster formation in a fumed-silica suspension involving steric interactions between silica particles by hydrogen bonded liquid solvation layers (dark green area surrounding particles). Hydrogen bonding possibilities between Aerosil 200 fumed-silica and PEG are represented in the inset image. Hydroxyl-terminated PEG ends and an isolated silanol on the particle surface as well as internal oxygen of PEG participate. Both silica and PEG can serve as hydrogen bond donors and acceptors.

density of oligomeric chains is higher than that of the bulk. As the temperature increases, the rate of dynamic exchange at the surface (the exchange between solvation layer and bulk) and the rate of diffusion of oligomer molecules increases. However, the solvation layer is always present at all temperatures investigated here.

The thickness and density of the solvation layer will significantly affect the shear-thickening responses, which is evident when comparing the results plotted for the PEG 200 and PEG 400 suspensions in Figure 3.5A and 3.5C, respectively where the critical shear rates decreased when the length of the polymer chains in the solvation layer was doubled. The thickness of the solvation layer will depend on the molecular weight of the oligomeric molecules, chain conformation, and nature of association between the oligomer chains and surface functional groups.[50-53] The solvation layer thickness was not measured for our systems but several observations can be made. The number of Kuhn segments (N) for a PEG 200 molecule is ~1.5 and Kuhn length (b) is 1.1 nm.[54] Thus, it seems unlikely that this molecule will form a loop, where both of the terminal glycol hydroxyl groups form simultaneous hydrogen bonds with the surface. PEG 200 molecules may align themselves along the fumed-silica surface forming –SiOH to ether group hydrogen bonds at one or more locations (Figure 3.8). Another possibility will be formation of hydrogen bonds between one terminal glycol hydroxyl and the silanol group at the surface. The fully extended length of PEG 200 chain is about 1.8 nm, whereas, the root mean square end-to-end distance ($R_0 = bN^{\frac{1}{2}}$) of a freely jointed PEG 200 chain is approximately 1.3 nm. Similarly, the fully extended chain length of PEG 400 is about 3.8 nm (approximately 3 Kuhn segments) and the root mean square end-to-end distance for PEG 400 is close to 1.9 nm. Similar to PEG 200, it is improbable that the PEG 400

chains will adapt and reach a fully extended conformation by hydrogen bonding of only one terminal glycol hydroxyl group to silanol groups (–SiOH) on the surface. Hence, loop formation is possible and would could result in a thinner solvation layer which would result in lessened steric interaction of particles approaching each other in a hydrocluster. Determining the exact conformational distribution and averages of oligomer chains in the surface solvation layer is beyond the scope of this work. But multiple hydrogen bonds likely exist on average between A200 silica and both PEG 200 and PEG 400 which would result in steric interactions of particles in close proximity.

Experimentally, the thickness of the adsorbed PEG layer on spherical silica particles have been estimated to be in the order of 1 nm.[51,52] Recently, He et al. used a magnetophotonic approach to determine the thickness of the solvation layer on silica coated Fe_3O_4 particles in water and in aqueous mixtures of organic solvents including methanol, ethanol, ethylene glycol, and diethylene glycol (DEG).[55] The solvation layer thickness in water is 4.4 nm, in 50% methanol is 4.1 nm, and in 50% ethanol is 3.5 nm. For 50% ethylene glycol (EG) the thickness is 1.8 nm, which further decreases to about 1.5 nm when the EG concentration was 90%. In comparison to EG, no significant difference was observed for DEG. PEG oligomers used in this study are expected to display behavior similar to DEG and EG. Based on these results,[51,52,55] the solvation layer thickness for PEG will be between 1 and 2 nm. When considering that the primary particle diameters of these fumed silica is ~12 nm, a solvation layer of such thickness would play a significant role in primary particle-to-primary particle interactions as two fumed silica particles come into close proximity.

R812 silica has a smaller surface density of silanol groups, ~0.44/nm^2, than A200 silica (~2.5/nm^2) and no isolated silanols.[48] Thus, R812 silica is less acidic (pH 5.5 to 7.5) compared to A200 silica (pH 3.7 to 4.7). Consequently, R812 silica forms fewer hydrogen bonds per unit surface area when dispersed in PEG and PPG due to less favorable hydrogen bonding. Steric shielding of some bridged silanol and siloxane groups by bulky trimethylsilyl groups further reduces hydrogen bonding and it also increases hydrophobicity. However, R812 silica gel formation (flocculation) in PPG 700 is prevented in part due to the small amount of hydrogen bonding that takes place between the particles and the fluid as well as hydrophobic-hydrophobic interactions occurring between the anchored t-butyl groups of the particles and the PPG, which has a lower oxygen to carbon ratio than the PEGs. These influences create more repulsive forces between particles in the 0.15 MF R812 in PPG 700 STF than in the PEG-based STFs leading to the more continuous shear thickening response as larger forces are required for R812 particles to come into close proximity.

PPG 700 oligomers are larger than PEG 200 and PEG 400, and, thus, the solvation layer thickness for PPG 700 could be thicker than those of the PEGs. It is anticipated that due to fewer hydrogen bonds and non-specific, hydrophobic-hydrophobic interactions the solvation layer of PPG will be less dense than those of PEG. This could have lowered the steric interaction of two approaching R812 particles compared to the A200 particles and led to the more continuous shear thickening of the behavior of the 0.15 MF R812 in PPG 700 samples.

3.3.4 Theoretical Analysis

Particle interactions, hence, hydrocluster formation and shear-thickening behavior, in these STFs is believed to be governed by a molecular force balance. Different types of interactions are acting on these systems in a complex manner. It is almost impossible to quantify the effect of individual interactions on the shear-thickening responses. This becomes further complicated as some of these interactions are a function of temperature. Here, we attempt to elucidate some of these interactions. As indicated by Raghavan et al.[42] the Hamaker constants of the fumed-silica and suspending media are very similar, particularly for PEG 200, resulting in negligible van der Waals forces. Therefore, van der Waals forces have been neglected from the molecular force balance governing the STFs in this study. It has also been postulated that the van der Waals forces between particles will not be significant and can be neglected in nonaqueous high particle concentration systems.[42]

During shearing deformation of suspensions, the relative motion between the suspending media and the particles causes particles to translate and rotate. As the shear rate increases, so too does the particle movement and the likelihood that two particles will approach one another. This causes a hydrodynamic lubrication force due to the flow of the suspending media out from the gap between two particles. If the particles have entered closed orbits, the force required to separate them is equal in magnitude to the force required bring them together. These forces are inversely proportional to the separation distance between the particles. The hydrodynamic force has been derived for two spheres approaching along their line of centers by determining the pressure field

obtained by solving the Stokes equation.[56,57] The pressure field can be integrated over the surface of one of the spheres,[26,58]

$$F_{hydrodynamic} = \frac{6\pi\eta_o a^3 \dot{\gamma}}{h} \quad 3.1$$

where, η_o is the zero-shear viscosity of the suspending media, a is the particle radius, $\dot{\gamma}$ is the shear rate, and h is the interparticle distance. Eq. 3.1 also describes the force required to separate two particles in close proximity where the suspending media would flow into the space vacated by the separating particles.

TEM micrographs (Figure 3.2) demonstrated that fumed-silica particles have fractal-like (branched) structures composed of multiple aggregated spherical particles. Therefore, Eq. 3.1 cannot be applied directly for fumed-silica systems. The corresponding functional form of the hydrodynamic force for the fractal-like particles is not known. However, we can assume that $F_{hydrodynamic}$ will have a somewhat similar functional form to that presented in Eq. 3.1, i.e.

$$F_{hydrodynamic} \sim f\left(\frac{\eta_o a_c^3 \dot{\gamma}}{h}\right) \quad 3.2$$

If a_c is chosen as the hydrodynamic radius of a fumed-silica particle and considering that the minimum distance between two nearest particles is equal to twice their hydrodynamic radius, the value of h will be very large, and the corresponding $F_{hydrodynamic}$ will be small. The repulsive forces would dominate the system and hydrocluster formation and the corresponding shear-thickening would not be significant. However, it is possible that specific segments (or branches) of a fumed-silica particle will be near to the segments of another particle, while at the same instant other parts of the particles can be far apart due to their branched nature. In that case, the hydrodynamic

force between two segments in the same vicinity becomes important. Here, a_c can be considered as the local size of the branches of the fumed-silica particle, which is related to the radius of the primary particles. It is anticipated that different segments of multiple particles interacting hydrodynamically on a local scale (Figure 3.8) could contribute to hydrocluster formation.

The interlocking of particle branches might play a role in keeping particles in close proximity, especially for interior particles of developed hydroclusters. Consider two approaching branched particles forming interlocks. Shearing of the suspending media would likely cause the particles to rotate and allow the interlocked branches to separate. Now consider a hydrocluster of many particles. Rotation of some particles, especially interior ones, might be restricted due to the combined interlocking of many particles' branches. This might prolong the coalesced configuration of a hydrocluster, which would be conceptually similar to the theoretical closed orbit of lubrication hydrodynamics that is part of the hydrocluster mechanism concept. The contribution to hydrocluster coalescence and growth due to the interlocking of particle branches would likely be a function of increasing shear rate due to the reliance on interlocking of interior particles of maintaining a hydrocluster configuration.

Recent simulation and experimental studies have reported that once the separation distance between particle surfaces is very small, a frictional contact force would arise proportional to the normal force.[32,35,40] However, in these studies the presence of a solvation layer, composed of suspending media molecules, present on particles' surfaces was not considered, and the particle volume-fractions employed in these studies were much greater than those used with the fumed-silica particles in our current work

(Table 1). We believe the solvation layer of suspending media present on our fumed-silica surfaces due to hydrogen bonding would likely preclude particle surface-to-surface contact, and ,hence, there would not be a frictional contact force in the traditional sense. If such contact occurs, particles, particularly A200, would form hydrogen bonds between themselves, and the particles would remain coalesced due to hydrogen bonding when the shear flow is removed. As a result, the shear-thickening process would be significantly less reversible. Our preliminary results indicate that the shear-thickening responses for the STFs considered here are mostly reversible. In a recent study, Liu et al. has shown that gelation due to particle surface-to-surface contacts takes place in STFs with higher concentrations of fumed-silica particles that are subjected to elevated temperatures (~80°C), where the chain exchange is high.[22] Furthermore, the shear-thickening behavior observed once this occurs is mostly continuous. We therefore consider that frictional forces may have some contribution towards the shear-thickening process but such contribution is not thought to be dominant.

With regard to repulsive forces, Brownian motion of suspended particles causes the particles to move away from each other. This counteracts hydrocluster formation. The Brownian force arises when the particles diffuse from a sheared configuration to a random configuration. Brownian forces ($F_{Brownian}$) scale with k_BT/a, where k_B is the Boltzmann constant, T is the temperature of the system, and a is the hydrodynamic radius.

The diffusivity D_0 of a single particle can be written as

$$D_o = \frac{k_B T}{6\pi\eta_o a} \tag{3.3}$$

where, a is considered to be the hydrodynamic radius of the fumed-silica particles, as the branches will not diffuse independently due to stiffness. Importantly, a is quite large for the fumed-silica particles considered here, so the corresponding D_0 will be small. The time scale associated with movement of a particle is $\sim\frac{a^2}{D_o}$. Larger a values and smaller D_0 can result in a larger time scales for particle diffusion. As temperature is reduced, the magnitude of D_0 also decreases. This will result in still slower diffusion at lower temperature. Thus, the suspended fumed-silica particles in oligomeric media in these STFs will experience only weak random motions that oppose hydroclustering and tend to increase the degree of shear thickening at lower temperatures.

Additionally, as the interparticle distance continues to decrease, a steric repulsive force is postulated to arise due to the compressive interaction of the approaching particles' solvation layers. This repulsive interaction becomes important when the interparticular distance is twice the solvation layer thickness since each particle has such a layer. Vincent et al. developed two repulsive potential functions for two approaching surfaces with strongly anchored polymer steric layers to describe the osmotic mixing of the anchored polymers with the suspending media as well as the elastic compression of the anchored polymers.[59] Differentiating these two potential functions with respect to interparticle distance leads to the force expressions. The steric repulsive force when two particles with surface-anchored polymers approach can be given by

$$F_{steric} = F_{elastic} + F_{mixing} \qquad 3.4$$

If the anchored-polymer is considered to be the hydrogen-bonded solvation layer, which is the same composition as the suspending media, the F_{mixing} term can be ignored. Based on Vincent et al.'s[59] formulation the steric force can then be written as

$$F_{steric} \sim \frac{a_c k_B T \delta \phi \rho}{M} g\left(\frac{h}{\delta}\right) \quad 3.5$$

where, ϕ is the volume-fraction of the suspending media contained in the solvation layers (equal to 1 for our case); δ is the solvation layer thickness; ρ is the suspending media density; M is the molecular weight of an oligomer chain of the suspending media; $g\left(\frac{h}{\delta}\right)$ is a non-dimensionalized functional form of interparticle distance, h. The F_{steric} component will be important as h approaches the value of 2δ. Similar surface interaction potentials have been proposed by others.[60,61]

In contrast to Vincent et al.'s[59] use of "strongly anchored" polymer chains,[43] the solvation layers of the A200 silica suspensions in PEG 200 and 400 will be composed of dynamically exchanging hydrogen-bonded suspending media only. These oligomers are not permanently covalently anchored. Now, the force required to perturb an ideal polymer chain is given by

$$f = \frac{3k_B T}{Nb^2} R \quad 3.6$$

where R is the chain end-to-end distance. Note that the deformation of an ideal polymer chain is represented by a spring, where $\frac{3k_B T}{Nb^2}$is the entropic spring constant. Interestingly, a chain becomes stiffer with increasing temperature. Now, the polymer chains in the solvation layer will not have their ideal bulk solution distribution of conformations and there will be small enthalpic effects during compression. However, the force required to compress these chains will have a similar functional form as Eq 6, i.e.,

$$force \sim spring\ constant * length\ solvation\ layer\ compression \quad 3.7$$

Note that Eqs. 5 and 6 are similar. Therefore the functional form given Eq. 3.5 can be used for our analysis.

The onset of shear-thickening occurs when the sum of all repulsive forces becomes equal to the sum of the forces acting to put and keep particles in close proximity

$$F_{Brownian} + F_{steric} \approx F_{hydrodynamic} + F_{friction} \quad 3.8$$

As discussed previously, friction, which is caused by particle to particle contact, is not a major factor, *i.e.,* $F_{friction} \approx 0$, at least over the temperature range considered here. The force component equations discussed above are simplified based on the interactions between only two particles. In a real system, interactions between multiple particles would need to be considered. However, the force balance would result in a form dimensionally similar to that given in Eq 8

$$\left[\frac{k_B T}{a} + \frac{a k_B T \delta \phi \rho}{M} g\left(\frac{h}{\delta}\right)\right] \sim f\left(\frac{{a_c}^3 \eta_o \dot{\gamma}_c}{h}\right) \quad 3.9$$

where, $\dot{\gamma}_c$ is the critical shear rate.

This phenomenological relationship (Eq. 3.9) can be investigated for the STFs considered in this study. The critical shear rates and associated critical shear stresses were estimated by determining the point at which the slope changes on the shear stress versus shear rate curves as shown in Figure 3.4B for each temperature tested. Also, the viscosities of the suspending liquids without dispersed fumed-silica were determined at each temperature. For the four STFs considered here, the critical shear rates and associated critical shear stresses determined for each experimental temperature were

plotted against the inverse of the pure suspending media's viscosity at that corresponding temperature (Figures 3.9A and 3.9B).

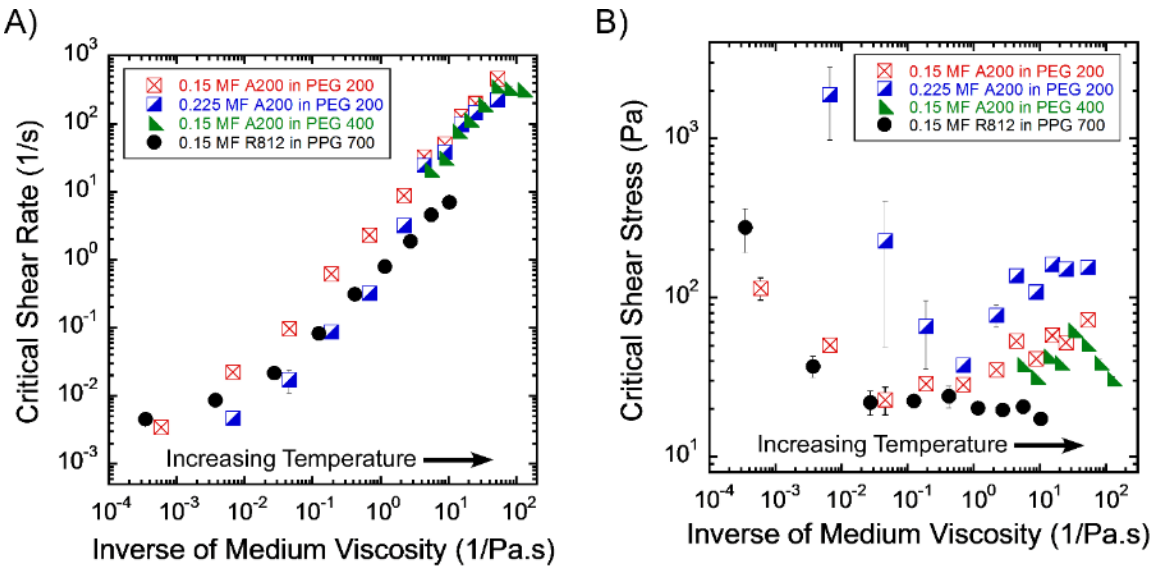

Figure 3.9 Critical shear rate and stress

Critical shear rate (A) and shear stress (B) values for four STFs plotted against the inverse of the pure suspending media viscosity for each experimental temperature.

Figure 3.9A demonstrates that the critical shear rates approximately scaled with the inverse of the viscosities of the pure suspending media, i.e, $\dot{\gamma}_c \sim {\eta_o}^{-1}$. A deviation from this relationship was observed at lower experimental temperatures. Similar observations have been made by Boersma et al. for various concentrated dispersions,[26] but only over a limited temperature range.

This shear rate and viscosity relationship also indicates that

$$\dot{\gamma}_c \eta_o = critical\ shear\ stress = a\ constant.$$

This can be obtained from the right side of Eq. 3.9, and considering that $\frac{{a_c}^3}{h}$ does not change. However, as shown in Figure 3.9B, the critical shear stress values vary with the

experimental temperature. The critical shear stresses for the PEG 200 and PPG 700 STFs drop rapidly as the reciprocal of viscosity increases (i.e., the viscosity decreases) and then rise for the two STFs dispersed in PEG 200 as the viscosity decreases further. The critical shear stress values for the PPG 700 level out and show no further increase as the viscosity continues to decrease. The critical shear stresses for 0.15 MF silica in PEG 400 do not show a sharp drop as the temperature was increased above the PEG 400 melting point. However, the experimental temperature range was limited for this case. This high variability in critical shear stresses further confirms that the onset of shear thickening is related to the critical shear rate and not the critical shear stress.

Near the melting point of PEG 200 and PPG 700, the critical shear stress values are high. It is likely that at those temperatures some kind of local order formation can take place in the suspending media, and due to this network-like structure the critical shear stress values are high. With increasing temperature, as viscosity decreases, such ordering disappears. Further increases of temperature resulted in increasing Brownian force and an increase of stiffness of the solvation layer. Therefore, a higher force is necessary to bring the particles close together for hydrodynamic coupling. Similar increases in critical shear stress has been reported by Mewis and Biebaut[27] with an increase in thickness of the stabilized layer as the temperature was increased. Similar to that study the critical shear stress values also increase with increasing concentration of suspended particles, which is again linked with the dense solvation layer. As discussed earlier, for the PPG system, the solvation layer is not as dense as those of the PEGs, and the corresponding force to deform the solvation layer does not change significantly with

increasing temperature. As a result, the critical stress almost remained constant with increasing temperature.

These results indicate that the shear-thickening behavior of a fluid can be tailored by varying the liquid and particle parameters. For instance, the isolated silanol groups of fumed-silica can be capped with various functional groups of different lengths and chemical compositions to modify their polarity, hydrogen bonding character, hydrophobicity, etc. Also, the suspending liquids can be polar or nonpolar, hydrophilic or hydrophobic, and hydrogen bonding or non-hydrogen bonding. The liquid can have higher or lower molecular weights, and its viscosity can be varied. All these factors can tailor the shear-thickening response and will be systematically studied in future publications. For instance, the critical shear rate can be increased by increasing the molecular weight of the suspending liquid.

3.4 Conclusions

The temperature-dependent shear-thickening behavior of four STFs consisting of fumed-silica and oxygen-containing oligomeric suspending media was investigated. A framework was advanced to support hydrocluster formation as the mechanism behind shear-thickening behavior for suspensions of fractal-shaped silica particles. Cluster formation is governed by a force balance among hydrodynamic, thermal, steric, and frictional forces.

Shear-thickening in these STFs, i) 0.15 MF A200 silica in PEG 200, ii) 0.225 MF A200 silica in PEG 200, iii) 0.15 MF A200 silica in PEG 400 and iv) 0.15 MF R812 silica in PPG 700, was shown to exist over a temperature range of approximately 100°C, beginning very near the melting point of suspending media. The critical shear rates

marking the onset of shear-thickening over the range of temperatures investigated were found to be inversely proportional to the viscosity of the pure suspending media at those same temperatures. Therefore, an expression for the temperature-dependent onset of shear-thickening should likely be based on the critical shear rate.

In general, reducing the temperature resulted in lower critical shear rates. Regardless of temperature, increasing the fumed-silica mass-fraction (MF) resulted in lower critical shear rates and an earlier onset of shear thickening. Higher MFs also resulted in behavior closer to discontinuous shear-thickening. Changing the particle surface chemistry and suspending media architecture (i.e., suspending trimethylsilicated R812 silica in PPG rather than A200 silica in PEG) greatly reduced the hydrogen bond density formed between the surface of the particles and the suspending media. This resulted in a significantly more continuous shear-thickening behavior. Small angle neutron scattering and ultra small angle neutron scattering experiments as a function of shear rate and temperature are were performed to discover direct evidence of hydrocluster microstructure formation (sizes and shapes) within the STFs. This will be addressed in the next chapter.

CHAPTER IV

SMALL ANGLE NEUTRON SCATTERING EXPERIMENTS OF FUMED SILICA BASED SHEAR THICKENING FLUIDS

4.1 Introduction

The viscosity of a complex fluid composed of particulates suspended in a liquid is often dependent on several factors such as temperature or shear rate. Shear thickening fluids (STFs) are complex fluids that can experience a remarkable rise in viscosity when sheared at a rate above a critical shear rate.[1,6,7,24,25] The STFs involved in this study will be discussed in detail later, but to demonstrate what rheological attributes make STFs notable consider Figure 4.1, which shows the rheological characterization of one of the STFs from this study. Over a shear rate range of 0.16 1/s to 100 1/s the sample exhibits shear thinning behavior which is common for many complex fluids wherein the viscosity of the sample decreases with increasing shear rate. During shear thinning the at-rest microstructure is re-oriented, and repulsive forces dominate the particles' movement causing them to align and to move past each other more easily, thus lowering the viscosity.[1] At shear rates higher than 100 1/s the sample exhibits shear thickening behavior wherein the viscosity rises dramatically with increasing shear rates. At and above the critical shear rate, the hydrodynamic drag forces acting on the particles overcomes the repulsive forces and leads to the formation of transient high particle density formations called hydroclusters causing the viscosity to rise.[1,7,25]

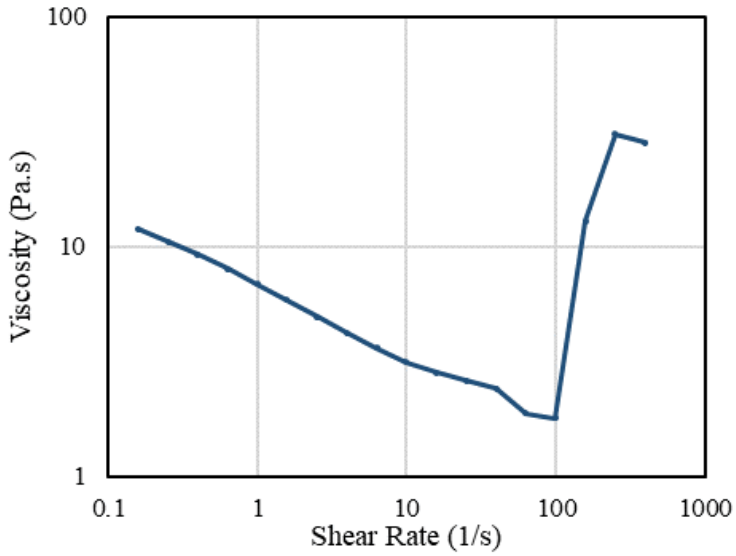

Figure 4.1 STF shear rate versus velocity curve

Viscosity versus shear rate data at 20°C for a 0.225 mass-fraction Aerosil 200 fumed silica in polyethylene glycol of 200 g/mol molecular weight

In a previous work, Warren et al. [20], the authors investigated the shear rate and temperature dependent behavior of STFs based on fumed silica particulate phases and showed evidence that the temperature dependent onset of shear thickening was a function of the critical shear rate, and that hydroclustering was the likely mechanism responsible for the shear thickening effect. This investigation sought to use small angle neutron scattering (SANS) to find further evidence of hydrocluster formation in those same samples. SANS is also seen as a suitable method for determining the surface and mass fractal dimensions of fractal-like aggregates such as fumed silica.[62]

SANS of static samples has been used to study the characteristics of fumed particles both dry as well as the microstructure formed they are when suspended in liquids or used as a filler in a solid system.[62-68] Suspensions of various particle and liquid systems have also undergone SANS experiments while the samples were under steady

shear rate conditions to investigate how their microstructures evolve with varying shear rates.[7,8,68-72]

Here SANS experiments were conducted on fumed silica based STFs from the previous work of Warren et al. at the National Institute of Standards and Technology's (NIST) Center for Neutron Research (NCNR). Steady shear experiments were conducted at 20°C for five STFs, each at multiple shear rates. A sixth STF underwent steady shear experiments at multiple shear rates over a temperature range of -40°C to 40°C. The shear rates at which the experiments were conducted were chosen separately for each STF to ensure that scattering data was collected during each STF's shear thinning region, at the critical shear rate, and within the shear thickening regime. An increase in scattering intensity was seen for all of the samples with increasing shear rate and across all temperatures in the low Q-range, approximately less than 0.01 1/A°. This indicates an evolution of the samples' microstructures consistent with the formation of hydroclusters.

4.2 Materials

The STFs investigated were based on one of two Aerosil fumed silicas, hydrophilic Aerosil 200 (A200) and hydrophobic Aerosil R812 (R812). They were suspended separately in one of three low molecular weight polar oligomeric glycols: hydroxyl-terminated polyethylene glycol either of molecular weight of 200 g/mol (PEG 200) or 400 g/mol (PEG 400) and a three-armed hydroxyl-terminated glycerol polypropylene oxide of molecular weight of 700 g/mol (PPG 700). The melting points of PEG 200, PEG 400, and PPG700 are -65°C, 6°C, and -32°C, respectively.

Fumed silicas are manufactured using a flame hydrolysis process wherein nearly spherical SiO_2 primary particles irreversibly fuse randomly into fractal-like branched

aggregates.[46] Smaller diameter primary particles result in aggregates with larger surface areas.[46] The primary particle diameter and specific surface area of A200 and R812 are ~12 nm and ~200 m^2/g and ~7 nm and ~260 m^2/g, respectively.[46-48] Lower surface area fumed silicas tend to form larger aggregates than higher surface area fumed silicas.[73] The characteristic lengths of the fumed silica particles used in this study are ~100-200 nm.

The majority of functional groups on the surface of A200 are silanols (-SiOH) that make A200 hydrophilic. R812 is based on Aerosil 300, which has a surface area of ~300 m^2/g and is also predominately covered with silanol groups.[46-48] The Aerosil 300 is aftertreated with hexamethyldisilazane which reduces the surface area to ~260 m^2/g and converts many of the surface silanol groups to trimethylsilyl groups ($-Si-(CH_3)_3$) rendering R812 hydrophobic.[46-48] The hydroxyl-terminated polymer chains of PEG 200 and PEG 400 readily form hydrogen bonds with the A200 particles due to the high surface density of silanol functional groups on A200. Relative to A200, R812 has a much smaller surface density of silanol groups that results in fewer hydrogen bonds leading to hydrophobic-hydrophobic interactions between the R812 particles. This causes the increase in viscosity after the critical shear rate to increase more slowly as the shear rate increases.

Table 4.1 gives an overview of the samples investigated including the type of fumed silica, the fumed silica mass-fraction (MF), the liquid phase, and the temperatures at which the experiments were performed. Four variants of the A200 in PEG 200 STF were investigated. Three varied the MF (0.1, 0.15, and 0.225) and the fourth was a 0.15 MF in PEG 200 that was treated with deuterium (D_20). Deuterating a sample tends to increase the intensity of the neutron scattering. Varying the molecular weight of the

suspending liquid was also investigated by suspending 0.15 MF A200 in PEG 400 instead of PEG 200. The final STF was an investigation of altering the liquid-particle interaction by dispersing hydrophobic R812 silica in PPG 700.

Table 4.1 Components of the STFs investigated

Fumed Silica	Mass-Fraction	Liquid Phase	Experiment Temperature
A200	0.1	PEG 200	20°C
A200	0.15	PEG 200	40°C, 20°C, 0°C, -20°C, -40°C
A200	0.15	D_2O treated PEG 200	20°C
A200	0.225	PEG 200	20°C
A200	0.15	PEG 400	20°C
R812	0.15	PPG 700	20°C

The fumed silicas were stored in a 105°C oven for a minimum of 24 hours prior to suspending them in the polar fluids to remove any moisture that had been absorbed by the fumed silicas' surface silanol functional groups. Each STF was produced using a Silverson L4RT-A high shear mixer to disperse the fumed silica in the polar fluid. The high shear mixer incorporated microbubbles into the STF requiring that each sample be degassed in a vacuum pot after mixing.

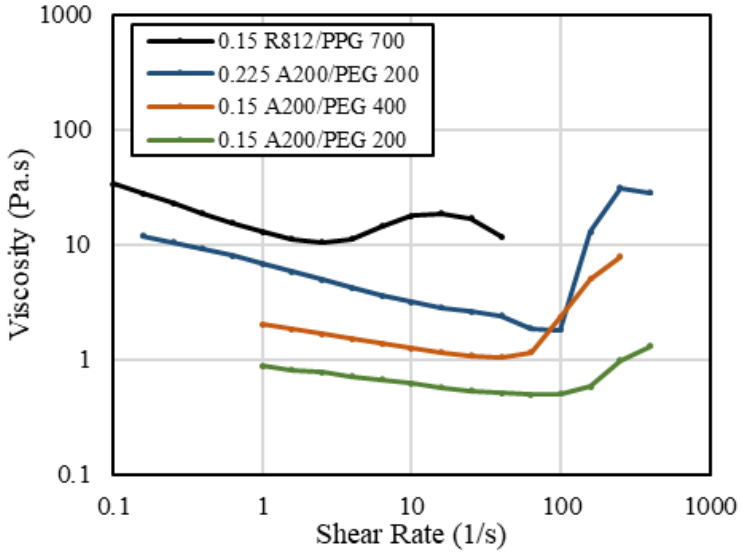

Figure 4.2 Shear rate versus velocity curve for four STFs

Viscosity versus shear rate data at 20°C for 0.15 mass-fraction (MF) Aerosil R812 fumed silica (R812) in glycerol polypropylene oxide of 700 g/mol molecular weight (PPG 700), 0.225 MF Aerosil 200 fumed silica (A200) in polyethylene glycol of 200 g/mol molecular weight (PEG 200), 0.15 MF A200 in polyethylene glycol of 400 g/mol molecular weight (PEG 400), and 0.15 MF A200 in PEG 200

Figure 4.2 shows the viscosity versus shear rate data at 20°C for 0.15 MF R812 in PPG 700, 0.225 MF A200 in PEG 200, 0.15 MF A200 in PEG 400, and 0.15 MF A200 in PEG 200. The data in Figures 4.2 and 4.3 were obtained using a TA Instruments Discovery Hybrid 2 rheometer using 25 mm diameter parallel plate fixtures with a 1 mm gap. Comparing the 0.225 and 0.15 MF A200 suspensions in PEG 200 it is evident that increasing the MF increases the viscosity of the sample, shortens the shear rate range over which the transition from shear thinning to shear thickening takes place, and increases both the magnitude and the rate of increase in the viscosity after the critical shear rate. Increasing the molecular weight of the A200 suspensions from PEG 200 to PEG 400 significantly reduces the critical shear rate, and similar to increasing the MF it also increases the magnitude of the shear thickening and how quickly it occurs. The 0.15

MF R812 in PPG 700 sample stands apart from the others because the particle-liquid interaction is changed from hydrogen bonding between a polar fluid and hydrophilic particles to predominately hydrophobic-hydrophobic particle interactions suspended in a polar fluid. This alteration in the particle-liquid interaction considerably increases the viscosity of the sample, reduces the critical shear rate, and reduces the rate of viscosity increase after the critical shear rate.

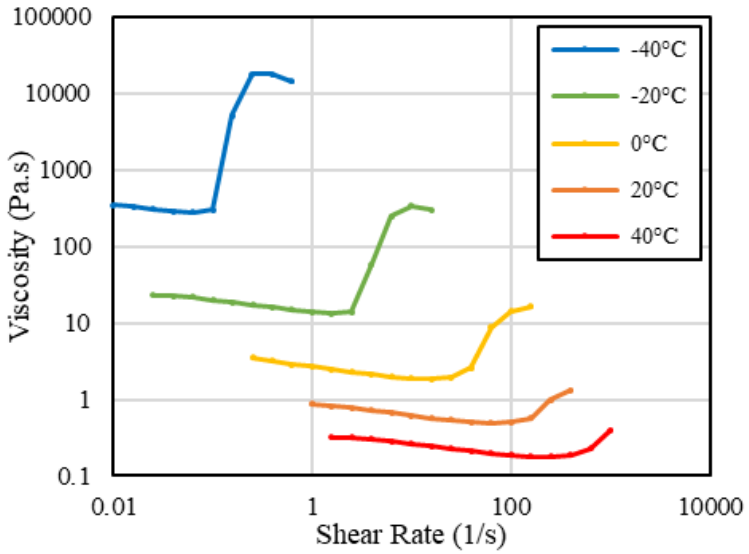

Figure 4.3 STF behavior over a temperature range, -40°C to 40°C

Viscosity versus shear rate data over a temperature range of -40°C to 40°C for 0.15 MF Aerosil 200 fumed silica in polyethylene glycol of 200 g/mol molecular weight

SANS experiments were performed on the 0.15 MF A200 in PEG 200 sample over a temperature range of -40°C to 40°C, and the corresponding viscosity versus shear rate curves for the sample over that temperature range are shown in Figure 4.3. Recall that the melting temperature of PEG 200 is -65°C. When the temperature of the sample is decreased, the initial viscosity increases, the critical shear rate is reduced, and similar

to increasing the MF of the particles or the molecular weight of the liquid the overall increase in viscosity and the rate at which it increases after the critical shear rate are significantly greater at lower temperatures.

4.3 Experimental Methods

The experiments were performed on the 30 meter long cold neutron SANS instrument on neutron guide NG7 at NCNR. Three different sample-to-detector distances were used to investigate a Q-range of 0.00112 1/A° to 0.2778 1/A°. The rheometer employed was an Anton Paar MCR-501 with a titanium Couette test fixture. The inner diameter of the Couette cup was 29 mm and the outer diameter of the Couette bob was 28 mm. An environmental chamber was fitted around the Couette fixture to regulate the temperature of the sample.

The Couette fixture was situated so that the incident neutron beam was aligned in the velocity gradient direction to collect scattering intensity data through the velocity-vorticity plane. This setup resulted in the neutron beam passing through the sample twice. Each STF underwent scattering experiments while under steady shear conditions at four to seven shear rates. These shear rates were chosen for each STF individually by considering the STF's shear rate versus viscosity curves in either Figure 4.2 or 4.3. As a minimum, at least one shear rate was chosen within the shear thinning and shear thickening regimes, as well as at the critical shear rate. There were 59 scattering experiments conducted in total. Each scattering experiment lasted approximately four hours, and a new sample was loaded for every experiment.

Maranzano and Wagner[5] found that during shear thickening for two high MF STFs (MF~0.5) the dominant scattering data in lower Q-ranges increased indicating the

formation of a larger number of structures at the larger length scales. Therefore, it was expected that the scattering data from this study would show an increase in scattering intensity at lower Q-ranges related to evolution of the STFs' microstructure indicative of the formation of hydroclusters. The effect of temperature on hydrocluster formation was investigated by conducting scattering experiments on the 0.15 MF A200 in PEG 200 sample at 40°C, 20°C, 0°C, -20°C, and -40°C. Scattering data for five other samples were collected at 20°C only and would be compared with the 0.15 MF A200 in PEG 200 scattering data at 20°C. One of these was a 0.15 MF A200 in PEG 200 that was treated with deuterium in an attempt to increase the scattering intensity. The other four samples were chosen to examine how three parameters effected microstructural evolution. First, the effect of varying the MF was examined with the SANS experiments on the 0.1 MF A200 in PEG 200 and 0.225 MF A200 in PEG 200 samples. Second, scattering data was collected for the 0.15 MF A200 in PEG 400 to see the effect of increasing the liquid's molecular weight from 200 g/mol to 400 g/mol. Third, the 0.15 MF R812 in PPG 700 results were used to investigate the initial microstructure and its evolution with increasing shear rate when the particle-liquid interaction was fundamentally altered.

4.4 SANS Results

The scattering data were reduced and corrected for the background and empty Couette cell scattering intensity using standard NCNR techniques in Igor Pro. The two-dimensional scattering intensity data was uniform for all azimuthal angles with no Bragg peaks indicating that there was no shear induced order.[8,70] Thus, the two-dimensional data was radially averaged. Maranzano and Wagner[7] found that the scattering intensity for a STF at rest and at low shear rates were virtually identical.

Therefore, no at-rest scattering data was collected due to the long scattering times and a tight beamline reservation schedule.

Figure 4.4 is intended to serve a demonstration for interpreting SANS data. Figure 4.4 shows scattering data for the 0.15 MF A200 in PEG 200 sample at the lowest and highest shear rates investigated for that sample, 1 1/s and 250 1/s, respectively. For Q-values greater than ~0.005 1/A°, which corresponds to length regimes smaller than ~20 nm, the two curves are very nearly indistinguishable. This indicates that the particles and microstructures are essentially identical for length scales smaller than ~20 nm, which corresponds approximately to the fumed silica primary particle length scales and would not be expected to change with increasing shear rate.[62,74]

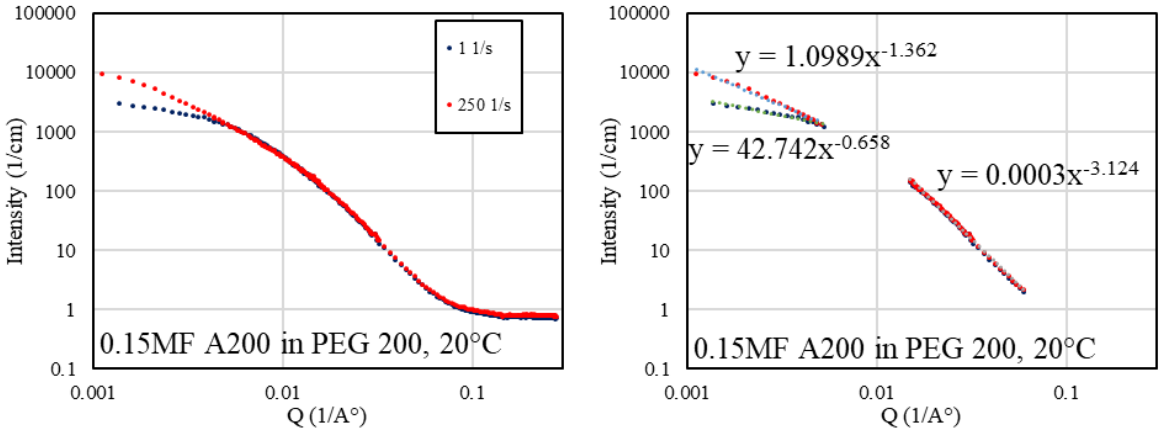

Figure 4.4 SANS analysis

Left) Scattering data at 20°C for the 0.15 MF A200 in PEG 200 sample at near at-rest conditions (shear rate of 1 1/s) and during advanced shear thickening (shear rate of 250 1/s), Right) Power law slopes of linear regions of the scattering data

The right plot of Figure 4.4 shows power law trendlines and their slope for linear regions of the scattering data for both shear rates in the low and high Q-ranges. The crossover point between these Q-ranges, the Guinier and Porod regions, corresponds to

the primary particle size of the fumed silica under static SANS.[62,73] The magnitude of the slope at Q-ranges larger than this crossover indicate the surface fractal dimension of the primary particles, and the slope at Q-ranges less than the crossover relate to the mass fractal dimension of larger aggregates.[62,66,73] A visual description of mass and surface fractals can be seen in Figure 4.5. The surface fractal dimension as described by Porod's law gives evidence of the smoothness of the particle surface; a value of 2 indicates a smooth surface while a value greater than 2 indicates a fractally rough surface.[67,73] Kawaguchi et al. [75] found that the surface fractal dimension of Aerosil 130 (A130) fumed silica was 3.2 indicating that the surface of the primary particles is fractally rough. The magnitude of the slope in the right plot in the higher Q-range (~0.015 1/A° to ~0.06 1/A°) indicates a surface fractal dimension for A200 of 3.12, which is the comparable to what Kawaguchi et al. found for A130.[75] Shaafer and Hurd[73] showed that the surface fractal dimension derived from static SANS experiments is independent of whether the fumed silica is dry or suspended in a liquid. The similarity between the surface fractal dimension determined by Kawaguchi et al. 75 and those found in this study suggests that the steady state shear conditions does not affect the surface fractal dimension.

The magnitude of the slope values of the right plot of Figure 4.4 in the lower Q-range (~0.001 1/A° to ~0.006 1/A°) show an increase in slope from 0.66 at the lowest shear rate to 1.36 at the highest shear rate. Narayanan et al. [67] note that slope values in the lower Q-ranges (Q<0.01 1/A°) of 2 or less are indicative of chain-like mass-fractal aggregates, which is consistent with the branched, fractal-like nature of the fumed silica particles. The increase in scattering intensity in the lower Q-range indicates microstructural evolution and the formation of larger structures, and the increase in the

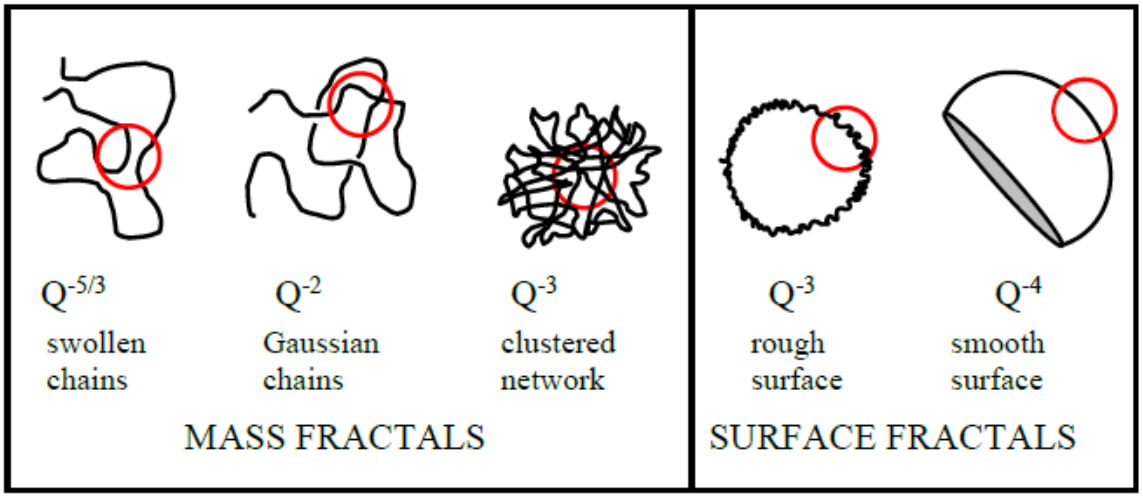

Figure 4.5 Mass and surface fractals[76]

Mass fractals (mass fractal dimension, D_m) are related to aggregates while surface fractals (surface fractal dimension, D_s) relate to the surface roughness of a particle

slope value shows an increase in the mass fractal dimension. Both of these facts are consistent with hydrocluster formation because the fumed silica particles themselves did not grow in size or alter their shape.

There is some slight non-linearity in Figure 4.4 in the lower Q-range for the lowest and highest shear rate. Non-linear scattering intensity data in the Guinier region at lower Q-ranges might indicate that the size of individual aggregates vary significantly.[77] The fact that Guinier's law doesn't hold for our samples might indicate that there is no single radius of gyration value. Linearity in the Guinier region would allow for a radius of gyration value to be determined, which would allow for an estimation of the size of the aggregate. This is reasonable for these fumed silica hydroclusters which are transient density fluctuations wherein particles are constantly joining or leaving the hydrocluster.

Figure 4.6 shows the scattering data for the deuterated 0.15 MF A200 in PEG 200 sample. This sample will be discussed as a representative of all but two of the samples that will be discussed later. The scattering data and mass and surface fractal dimension slope breakdowns for all of the samples and experiments can be seen in the Supplemental Data section at the end of this chapter. The scattering intensity in the higher Q-range roughly above 0.007 1/A° at all shear rates are nearly indistinguishable because this region is related to the length scale of the primary particles. This indicates that the size and surface fractal dimension of the primary particles is very consistent.

In the lower Q-range (~0.001 1/A° to ~0.006 1/A°) there is a definite increase in scattering intensity with increasing shear rate. Deuterating the sample magnified the scattering intensity. This increase in scattering intensity occurs even at shear rates in the shear thinning regime consistent with a changing microstructure as the particles realign so as to move past each other in the flow. The critical shear rate for this sample was 127 1/s. The scattering data for the two higher shear rates, 250 1/s and 500 1/s, are markedly higher that at the critical rate, which is likely evidence of hydrocluster formation.

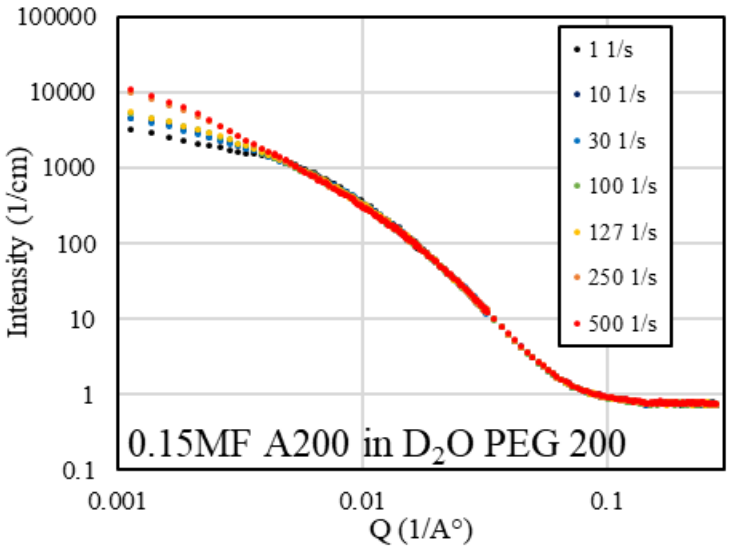

Figure 4.6 Scattering data at 20°C for deuterated 0.15 MF A200 in PEG 200

The scattering data for the 0.15 MF R812 in PPG 700 STF seen in Figure 4.7. This sample was unique in this study as it was the only sample based on the hydrophobic R812 fumed silica. The initial microstructure of this sample was dominated by hydrophobic-hydrophobic particle interactions, which resulted in a viscous gel-like equilibrium state. The evidence of this gel-like state can be seen in the scattering data for the lowest shear rate for which it was tested, 0.1 1/s. As the shear rate is increased, the dominance of the hydrophobic-hydrophobic interactions is lessened, and the scattering intensity becomes consistent with the data from the other samples. The critical shear rate for this sample was 2 1/s, and although the microstructure is definitely evolving there is no marked increase in the scattering intensity at the higher shear rates. This is consistent with the more continuous nature of this sample's shear thickening response seen in Figure 4.2.

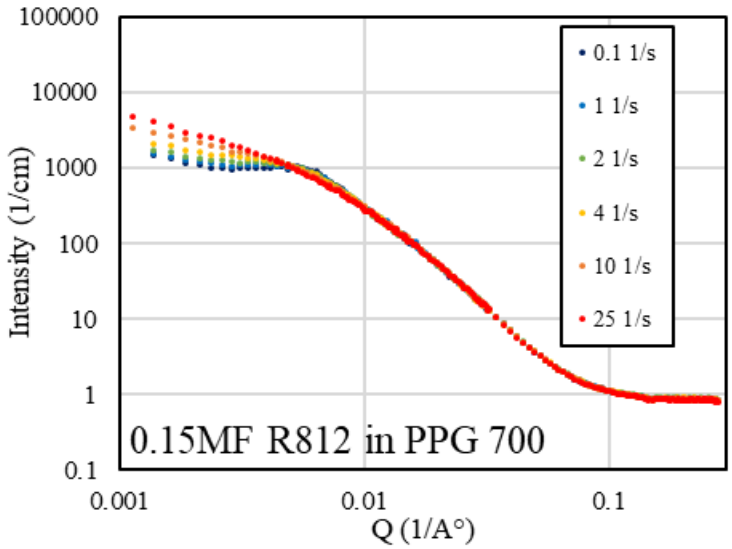

Figure 4.7 Scattering data at 20°C for 0.15 MF R812 in PPG 700

The scattering result was that for the 0.225 MF A200 in PEG 200 STF seen in Figure 4.8. This STF showed some of the most dramatic shear thickening behavior of all the samples during the parallel plate steady shear experiments, the results of which can be seen in Figure 4.2. The scattering intensity data in Figure 4.8 unexpectedly shows only a modest evolution of the microstructure. The data does, however, have the largest regions of linearity in the scattering data at the low Q-range. This suggests that there might be another shear thickening mechanism occurring in addition to hydroclustering. STFs based on fumed silica have a higher effective MF due to the inclusion of the bulk liquid within the interstitial spaces in the hydrocluster, which might indicate that be particle interaction similar to jamming of close packed particles in addition to hydroclustering.

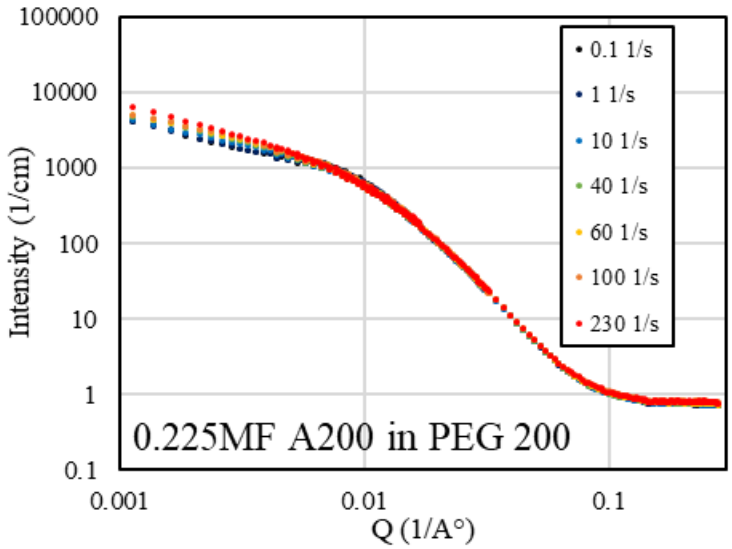

Figure 4.8 Scattering data at 20°C for 0.225 MF A200 in PEG 200

The mass and surface fractal dimensions for all the STFs are given in Table 4.2. The slope values were determined for each sample in the same manner as in Figure 4.4, and the scattering plots for each sample can be seen in the Supplemental Data at the end of this chapter. The surface fractal dimensions are in the High Q-range column, and the comparable values for all of the A200 based STFs confirms the consistent size and shape of the A200 primary particles. The slightly lower value for the R812 STF might indicate a slightly smoother surface. The Low Q-range columns give the mass fractal dimension for each STF at both the lowest and highest shear rate experiments. These rates would be near equilibrium and during shear thickening, respectively. The low shear rate mass fractal dimensions are consistent for all the A200 STFs except for the 0.1 MF A200 in PEG 200 sample, and it is not clear why this sample seems to be an outlier (the first sample listed in Table 4.2). There is no mass low shear rate fractal dimension for the

R812 STF as it's equilibrium gel-like microstructure was dominated by hydrophobic-hydrophobic particle interactions.

There is a consistent trend in the mass fractal dimensions for the STFs based on A200 in PEG 200, the first four lines in Table 4.2. Narayanan et al.[67] note that slope values in the lower Q-ranges (Q < 0.01 1/A°) of 2 or less are indicative of chain-like mass-fractal aggregates. As the MF is increased, the mass fractal dimension is reduced. This might indicate that the structures being formed inside the flow become more fractal-like with higher MFs. The deuterated sample (the third sample listed in Table 4.2) is an outlier likely due to its treatment with deuterium, which replaced terminal hydrogens with deuterium leading to an increase in scattering intensity. The mass fractal dimensions for the PEG 400 and PPG 700 samples are likely related to the liquid particle interactions of those STFs, but no comparison can be made without results from other versions of those STFs. It's possible that the higher mass fractal dimension of the PEG 400 sample is related to the longer polymer chains of the suspending liquid.

Table 4.2 Mass and surface fractal dimensions for all samples at 20°C

		Low Q-range				High Q-range
STF	Temp	Lowest Shear Rate	D_m	Highest Shear Rate	D_m	D_s
0.1 MF A200 in PEG 200	20°C	10 s^{-1}	1.26	2000 s^{-1}	1.82	3.01
0.15 MF A200 in PEG 200	20°C	1 s^{-1}	0.66	250 s^{-1}	1.36	3.12
0.15 MF A200 in D2O PEG 200	20°C	10 s^{-1}	0.72	500 s^{-1}	1.60	3.08
0.225 MF A200 in PEG 200	20°C	0.1 s^{-1}	0.73	230 s^{-1}	0.97	3.19
0.15 MF A200 in PEG 400	20°C	1 s^{-1}	0.67	300 s^{-1}	1.79	3.10
0.15 MF R812 in PPG 700	20°C	0.1 s^{-1}	--	025 s^{-1}	1.09	2.86

A varying temperature study was conducted for the 0.15 MF A200 in PEG 200 STF, and the resulting mass and surface fractal dimensions are given in Table 4.3. The surface fractal dimensions in the High Q-range column again are very similar confirming the consistency of the size and shape of the primary particles. In the Low Q-range column, the lowest shear rate mass fractal dimensions are also comparable. This is expected as each sample came from the same 0.15 MF A200 in PEG 200 batch. Any variance in the in these initial mass fractal dimensions is related to the experiment's shear rate. The high shear rate mass fractal dimension shows a consistent trend of increasing mass fractal dimension with increasing temperature indicating that larger aggregates are likely being formed in the higher temperature samples. This might indicate that the aggregates are decreasing in size as the temperature decreases.

Table 4.3 Mass and surface fractal dimensions for the temperature study

		Low Q-range				High Q-range
STF	Temp	Lowest Shear Rate	D_m	Highest Shear Rate	D_m	D_s
0.15 MF A200 in PEG 200	40°C	10 s^{-1}	0.78	750 s^{-1}	1.52	3.10
0.15 MF A200 in PEG 200	20°C	1 s^{-1}	0.66	250 s^{-1}	1.36	3.12
0.15 MF A200 in PEG 200	0°C	1 s^{-1}	0.68	10 s^{-1}	1.30	3.13
0.15 MF A200 in PEG 200	-20°C	0.1 s^{-1}	0.65	5 s^{-1}	1.27	3.11
0.15 MF A200 in PEG 200	-40°C	0.01 s^{-1}	0.63	0.1 s^{-1}	0.75	3.11

4.5 Conclusion

The results of the SANS steady state rheological characterization experiments performed on all of the STF samples in this study showed strong evidence of microstructural evolution with increasing shear rates at length scales larger than the

primary particle size of the fumed silica. These changes in the microstructure support the premise of the hydroclustering mechanism being the causation of the shear thickening phenomenon. Another result of these experiments was the confirmation that the size and shape of the primary particles is very consistent based on the higher Q-range data for the samples being almost indistinguishable across shear rates and samples.

The NCNR suggests using SasView for analyzing and fitting SANS data, but none of the existing physics based models in SasView could be made to fit the scattering data in this study when the using known physical dimensions of these fumed silica particles and the suspending fluids were input. Therefore, only the mass and surface fractal dimensions could be analyzed using linear portions of the scattering intensity data as seen in Figure 4.4. The surface fractal dimensions across all of the A200 samples were similar and comparable to what has been reported in the literature, which again confirms the consistent size and shape of the primary particles.

The mass fractal dimension during shear thickening decreased with increasing MF possibly indicating that the shear thickened microstructure is more fractal-like at higher particle loadings. However, the scattering intensity results for the 0.225 MF A200 in PEG 200 showed unexpected low microstructural evolution during shear thickening indicating that an additional shear thickening mechanism might be occurring in this sample such as jamming of close packed particles due to the larger effective MF of fumed silica based STFs. The varying temperature study showed that the shear thickened mass fractal dimension decreased with decreasing temperature, which might indicate that the smaller aggregates are being formed at lower temperatures. Although this study has shown definitive microstructural evolution during shear thickening believed to be

consistent with the hydroclustering mechanism, the few unexpected results of this study could be further investigated with additional experiments including an estimation of the effective MFs of these fumed silica suspensions and investigating the initial gel-like microstructure of the 0.15 MF R812 in PPG 700 STF.

4.6 Supplemental Data

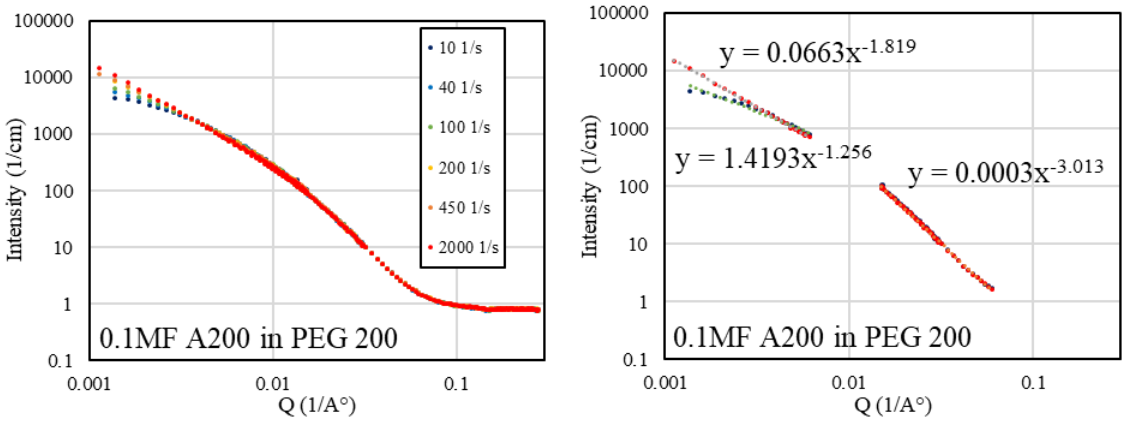

Figure 4.9 Scattering data at 20°C for 0.1 MF A200 in PEG 200

Left) data for all shear rates investigated, Right) power law slopes for the highest and lowest shear rates

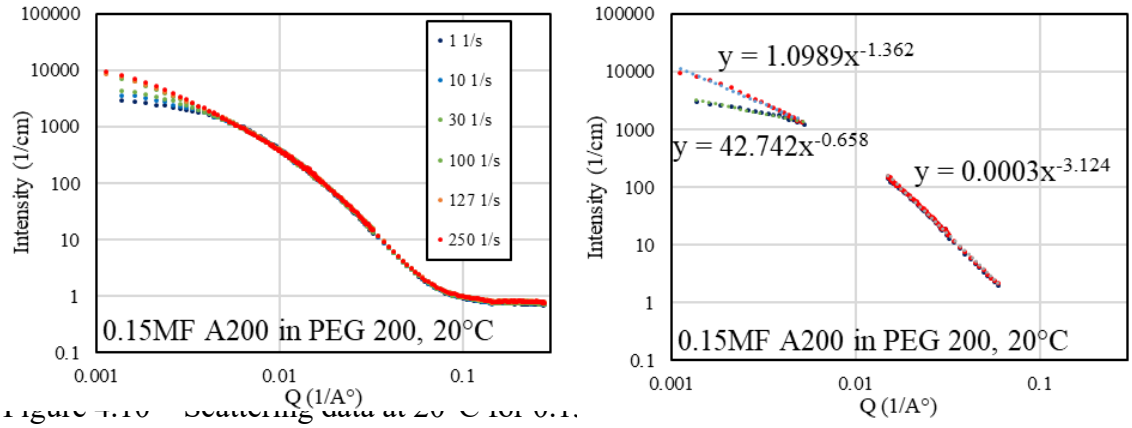

Left) data for all shear rates investigated, Right) power law slopes for the highest and lowest shear rates

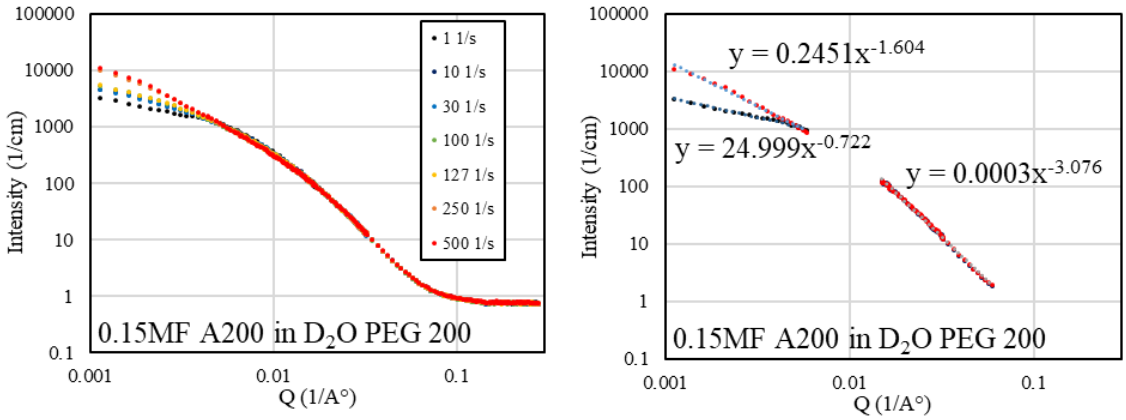

Figure 4.11 Scattering data at 20°C for deuterated 0.15 MF A200 in PEG 200

Left) data for all shear rates investigated, Right) power law slopes for the highest and lowest shear rates

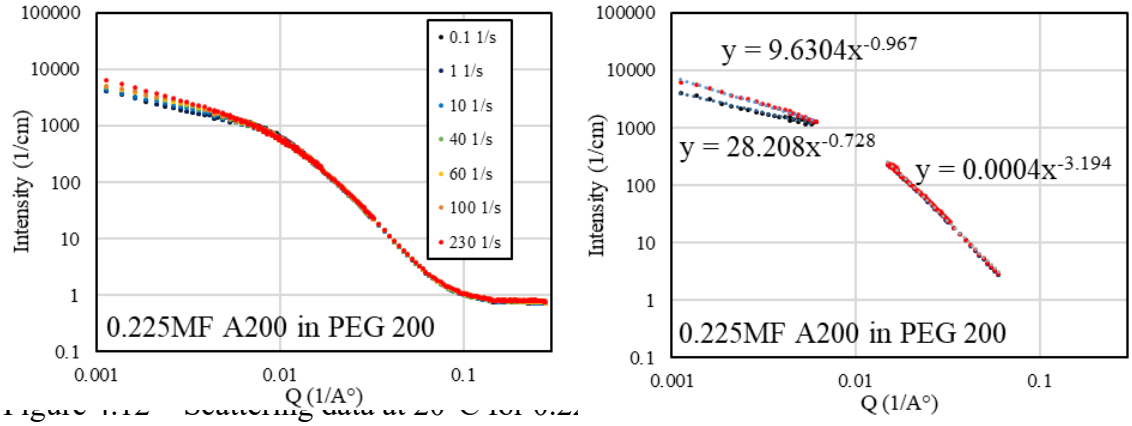

Left) data for all shear rates investigated, Right) power law slopes for the highest and lowest shear rates

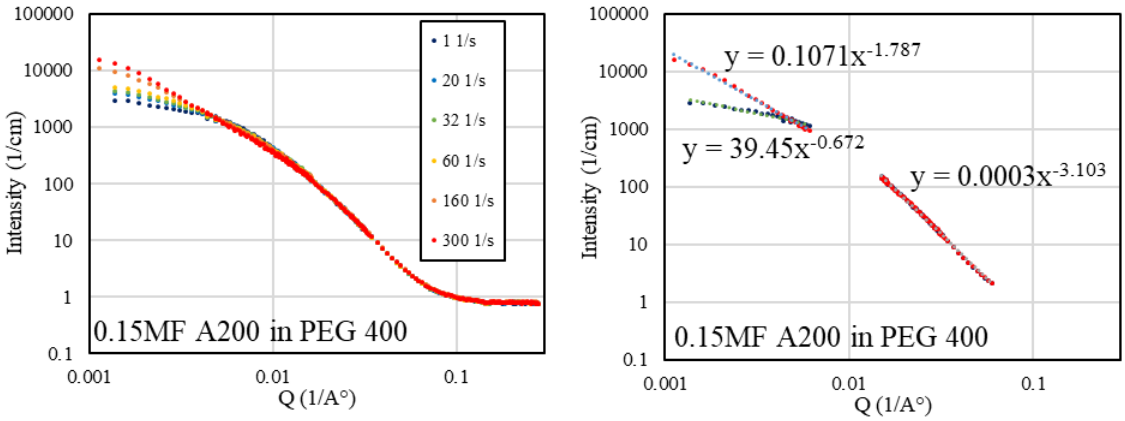

Figure 4.13 Scattering data at 20°C for 0.15 MF A200 in PEG 400

Left) data for all shear rates investigated, Right) power law slopes for the highest and lowest shear rates

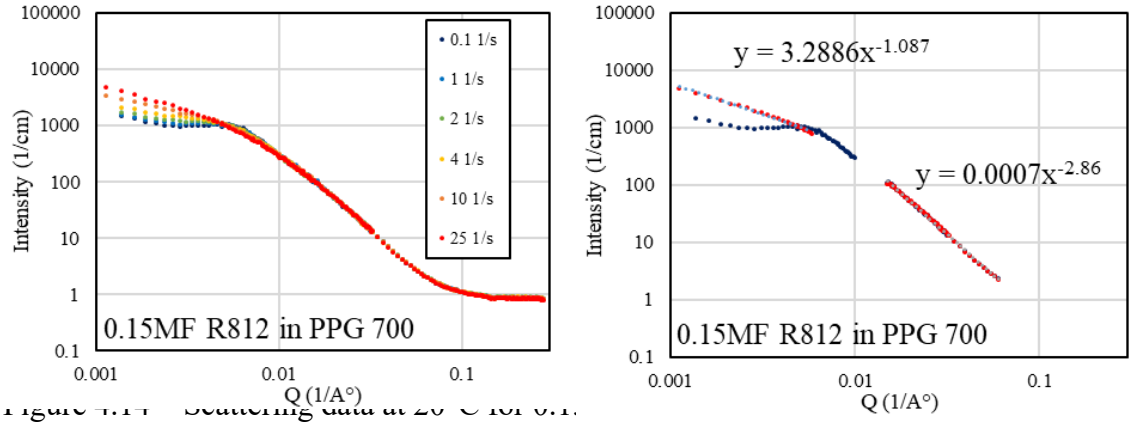

Left) data for all shear rates investigated, Right) power law slopes for the highest and lowest shear rates

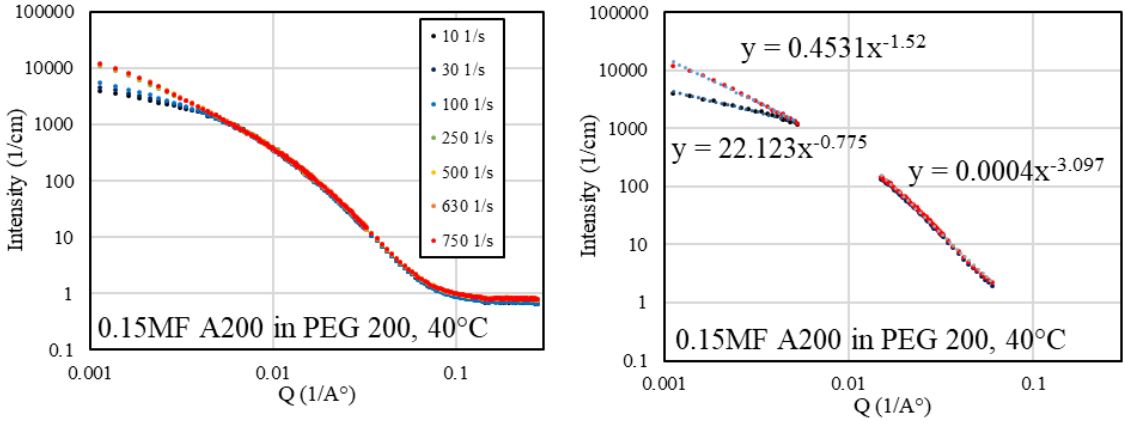

Figure 4.15 Data for 0.15 MF A200 in PEG 200 at 40°C

Left) data for all shear rates investigated, Right) power law slopes for the highest and lowest shear rates

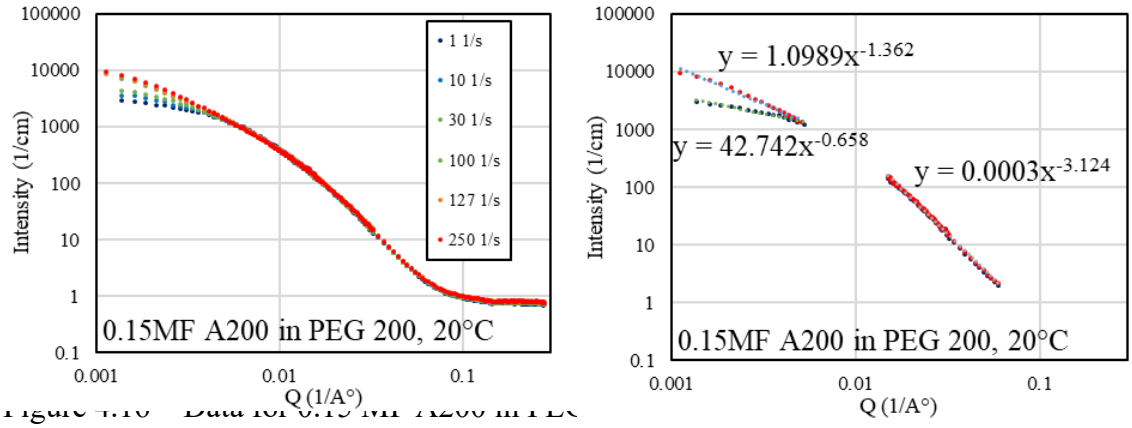

Left) data for all shear rates investigated, Right) power law slopes for the highest and lowest shear rates

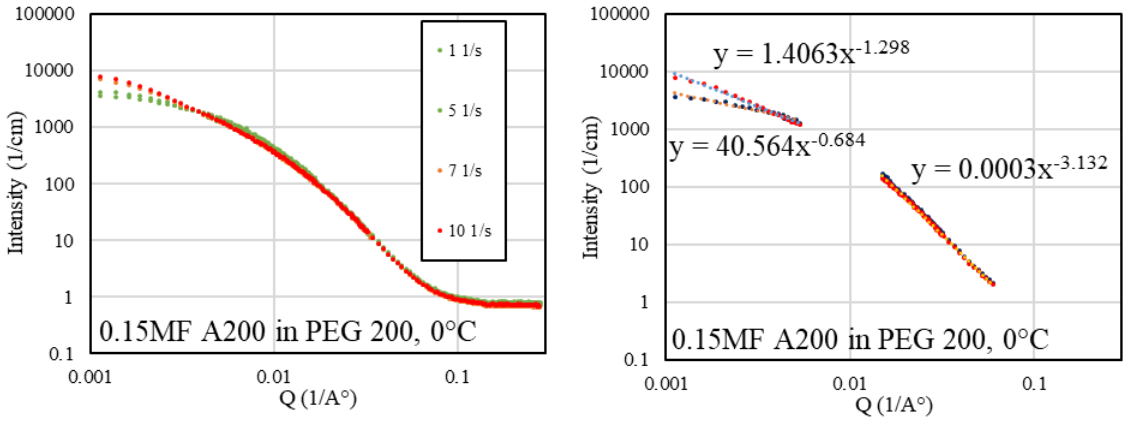

Figure 4.17 Data for 0.15 MF A200 in PEG 200 at 0°C

Left) data for all shear rates investigated, Right) power law slopes for the highest and lowest shear rates

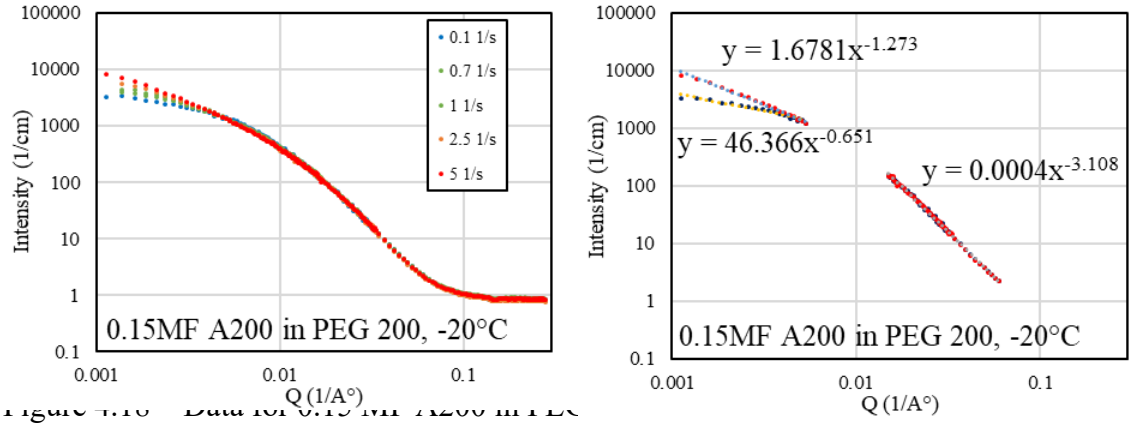

Left) data for all shear rates investigated, Right) power law slopes for the highest and lowest shear rates

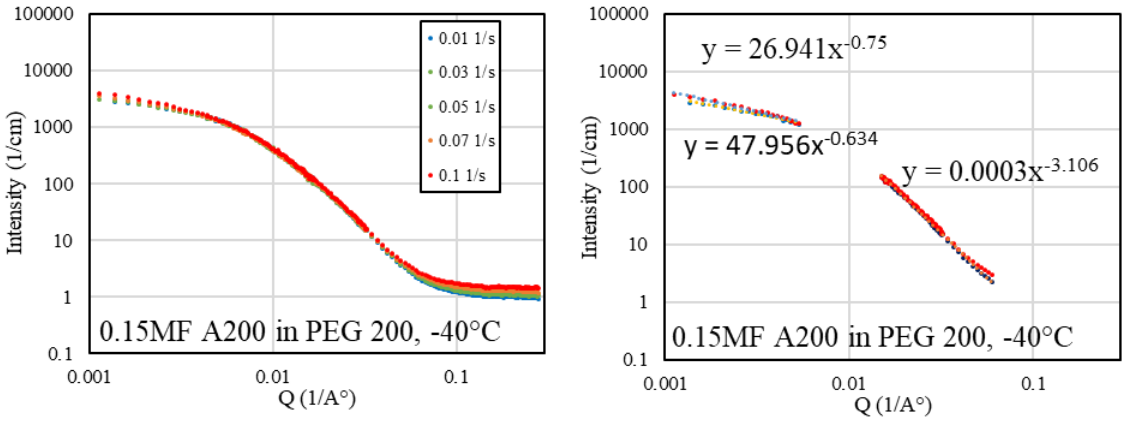

Figure 4.19 Data for 0.15 MF A200 in PEG 200 at -40°C

Left) data for all shear rates investigated, Right) power law slopes for the highest and lowest shear rates

CHAPTER V

CONCLUSIONS

These studies initially focused on an investigation of novel MMOD shielding concepts. It was decided that a sandwich panel with a porous core could be imbibed with a STF due its shear rate dependent behavior. This in turn led to a further study on characterizing the rheological shear rate and temperature dependent behavior of fumed silica-based STFs using rheometers and probing their microstructural evolution with increasing shear rate.

The spacecraft MMOD shieling concept of a metallic sandwich panel with a honeycomb core filled with a STF showed promise in preventing perforation of the rear facesheet, as well as reducing the amount of damage to the core structure when subjected to HVI experiments. The room temperature HVI experiments of identical panels filled with the STF liquid phase only resulted in perforation of the rear facesheet and significantly more core damage. This likely means that the STF filled panel would have retained more of its structural strength than the panel filled with the liquid phase alone.

Filling the honeycomb cells required two cure cycles that resulted in a weaker bond strength of one facesheet due to a portion of the adhesive flowing into the STF. The orientation of this facesheet, whether impact-side or rear-side, was shown to greatly affect the nature of the core damage and to a lesser extent deformation of the facesheets. The lower temperature experiments caused embrittlement of the facesheet adhesive and

resulted in much greater delamination of the facesheet with the weaker bond. However at the low temperature the damage to the core was lessened.

Analysis of these results could go on to include hydrocode simulations of the HVI experiments in an effort to replicate the nature and extent of damage seen in the experimental results. More concepts could also be produced incorporating a STF filled layer into a multi layer concept.

The rheological characterization of the fumed silica and polar oligomer STFs used in this study showed shear thinning and shear thickening behavior over a wide range in temperatures including just above the liquids' melting points. More importantly, the functional form of the expression for determining the temperature dependent onset of shear thickening was shown to much more likely be a function of the critical shear rate rather than the critical shear stress.

The mechanism responsible for the shear thickening behavior is believed to be the formation of hydroclusters, and this evolution of the suspensions' microstructures seems to be evident from the SANS experiments. There the scattering intensity increased in the low Q range with increasing shear rate indicating a change in the microstructure at length scales larger than the particle sizes. Recall that the scattering intensity data seen in Chapter 4associates the number of neutrons deflected off of elements of the suspensions; microstructures that impacted the detector. The increase in scattering intensity was seen at length scales larger than the individual fumed silica particles' characteristic length, which gave strong evidence of the hydroclustering mechanism occurring. However, the SANS results could not be fit with any existing physics-based model used for characterizing fractal like particles. The scattering intensity was also shown to vary with

temperature becoming greater at higher temperature. Further work could be performed to investigate the behavior of other STFs with varying particles or even combing particle types. Furthering our understanding of STFs could one day lead to a STF or STF-like material being integrated into an actual MMOD shielding concept, and this work lends credence to using fumed silica as the particulate due to the strong shear thickening behavior that shown at relatively small MFs and evidence of hydroclustering.

REFERENCES

(1) Wagner, N. J.; Brady, J. F. Shear Thickening in Colloidal Dispersions. *Physics Today* **2009,** *62* (10), 27-32.

(2) Reynolds, O. Lvii. On the Dilatancy of Media Composed of Rigid Particles in Contact. with Experimental Illustrations. *The London, Edinburgh, and Dublin Philosophical Magazine and Journal of Science* **1885**, *20* (127), 469-481.

(3) Einstein, A. "A New Determination of Molecular Dimensions. *Ann. Phys*. **1906**, *19* (2), 289-306.

(4) Bagnold, R.A. Experiments on a Gravity-free Dispersion of Large Solid Spheres in a Newtonian Fluid Under Shear. *Proceedings of the Royal Society of London A: Mathematical, Physical and Engineering Sciences* **1954**, *225* (1160), 49-63.

(5) Metzner, A.B.; Whitlock, M. Flow behavior of concentrated (dilatant) suspensions. *Transactions of The Society of Rheology,* **1958**, *2* (1), 239-254.

(6) Barnes, H.A. Shear-Thickening ("Dilatancy") in Suspensions of Nonaggregating Solid Particles Dispersed in Newtonian Liquids. *Journal of Rheology* **1989**, *33* (2), 329-366.

(7) Maranzano, B.J.; Wagner, N. J. Flow-small angle neutron scattering measurements of colloidal dispersion microstructure evolution through the shear thickening transition. *The Journal of Chemical Physics* **2002**, *117* (22), 10291-10302.

(8) Lee, Y.S.; Wagner, N.J. Rheological properties and small-angle neutron scattering of a shear thickening, nanoparticle dispersion at high shear rates. *Industrial & Engineering Chemistry Research* **2006**, *45* (21), 7015-7024.

(9) Lee, Y. S.; Wetzel, E. D.; Wagner, N. J. The Ballistic Impact Characteristics of Kevlar® Woven Fabrics Impregnated with a Colloidal Shear Thickening Fluid. *J. Mater. Sci.* **2003**, *38* (13), 2825-2833.

(10) Fischer, C.; Braun, S. A.; Bourban, P.-E.; Michaud, V.; Plummer, C. J. G.; Månson, J. E. Dynamic Properties of Sandwich Structures with Integrated Shear-Thickening Fluids. *Smart Mater. Struct*. **2006**, *15* (5), 1467-1475.

(11) Warren, J.; Cole, M.; Offenberger, S.; Lacy, T. E.; Toghiani, H.; Burchell, M.; Kundu, S.; Pittman, C. U. Hypervelocity Impact of Honeycomb Core Sandwich Panels Filled with Shear Thickening Fluid. In *28th Technical Conference of the American Society for Composites*; Penn State University, 2013; pp 124–135.

(12) Tribble, A. C. *The Space Environment,* Princeton University Press: Princeton, 2003.

(13) Pisacane, V.L. *The Space Environment and Its Effects on Space Systems,* AIAA: Reston, 2008.

(14) Whipple, F. L. Meteorites and Space Travel. *Astr. J.* **1947,** *52*, 131.

(15) Cour-Palais, B. G.; Crews, J. L. A Multi-shock Concept for Spacecraft Shielding. *Int. J. of Imp. Engng*. **1990,** *10* (1-4), 135-146.

(16) Christiansen, E. L.; Kerr, J. H. Mesh Double-bumper Shield: a Low-weight Alternative for Spacecraft Meteoroid and Orbital Debris Protection. *Int. J. of Imp. Engng*. **1993,** *14*, 169-180.

(17) Christiansen, E. L.; Crews, J. L.; Williamsen, J. E.; Robinson, J. H.; Nolen, A. M. Enhanced Meteoroid and Orbital Debris Shielding. *Int. J. of Imp. Engng*. **1995,** *17*, 217-228.

(18) Zukas, J. A.; Nicholas, T.; Swift, H. F.; Greszczuk, L. B.; Curran, D. R. *Impact Dynamics*, J. Wiley: New York, 1982.

(19) Ryan, S. J.; Christiansen, E. L.; Lear, D. M. Development of the Next Generation of Meteoroid and Orbital Debris Shield. In *AIP Conference Proceedings* **2009**, *1195* (1), 1417-1420.

(20) Warren, J.; Offenberger, S.; Toghiani, H.; Pittman, C.U.; Lacy, T.E., Kundu, S. Effect of Temperature on the Shear-Thickening Behavior of Fumed Silica Suspensions. *ACS Applied Materials and Interfaces* **2015,** *7* (33), 18650-18661.

(21) Cheng, X.; McCoy, J. H.; Israelachvili, J. N.; Cohen, I.; Imaging the Microscopic Structure of Shear Thinning and Thickening Colloidal Suspensions. *Science* **2011,** *333*, 1276-1279.

(22) Liu, X.Q.; Bao, R.Y.; Wu, X.J.; Yang, W.; Xie, B.H.; Yang, M.B. Temperature Induced Gelation Transition of a Fumed Silica/PEG Shear Thickening Fluid. *RSC Advances* **2015,** *5* (24), 18367-18374.

(23) Burchell, M.J.; Cole, M.J.; McDonnell, J.A.M.; Zarnecki, J.C. Hypervelocity Impact Studies Using the 2 MV Van de Graaff Dust Accelerator and Two Stage Light Gas Gun of the University of Kent at Canterbury *Meas. Sci. Tech*. **1999,** *10*, 41-50.

(24) Brown, E.; Jaeger, H. M. Shear Thickening in Concentrated Suspensions: Phenomenology, Mechanisms and Relations to Jamming. *Rep. Prog. Phys.* **2014**, *77*, 046602–1–23.

(25) Mewis, J.; Wagner, N. J. *Colloidal Suspension Rheology*; Cambridge University Press: Cambridge; New York, 2013.

(26) Boersma, W. H.; Laven, J.; Stein, H. N. Shear Thickening (dilatancy) in Concentrated Dispersions. *AIChE J.* **1990**, *36*, 321–332.

(27) Mewis, J.; Biebaut, G. Shear Thickening in Steady and Superposition Flows Effect of Particle Interaction Forces. *J. Rheol.* **2001**, *45*, 799.

(28) Hoffman, R. L. Discontinuous and Dilatant Viscosity Behavior in Concentrated Suspensions. I. Observation of a Flow Instability. *Trans. Soc. Rheol.* **1972**, *16*, 155–173.

(29) Hoffman, R. L. Discontinuous and Dilatant Viscosity Behavior in Concentrated Suspensions. II. Theory and Experimental Tests. *J. Colloid Interface Sci.* **1974**, *46*, 491–506.

(30) Foss, D. R.; Brady, J. F. Structure, Diffusion and Rheology of Brownian Suspensions by Stokesian Dynamics Simulation. *J. Fluid Mech.* **2000**, *407*, 167–200.

(31) Kalman, D. P.; Wagner, N. J. Microstructure of Shear-Thickening Concentrated Suspensions Determined by Flow-USANS. *Rheol. Acta* **2009**, *48*, 897–908.

(32) Mari, R.; Seto, R.; Morris, J. F.; Denn, M. M. Shear Thickening, Frictionless and Frictional Rheologies in Non-Brownian Suspensions. *J. Rheol.* **2014**, *58*, 1693–1724.

(33) Fernandez, N.; Mani, R.; Rinaldi, D.; Kadau, D.; Mosquet, M.; Lombois-Burger, H.; Cayer-Barrioz, J.; Herrmann, H. J.; Spencer, N. D.; Isa, L. Microscopic Mechanism for Shear Thickening of Non-Brownian Suspensions. *Phys. Rev. Lett.* **2013**, *111*, 108301–1– 5.

(34) Heussinger, C. Shear Thickening in Granular Suspensions: Interparticle Friction and Dynamically Correlated Clusters. *Phys. Rev. E* **2013**, *88*, 050201–1 –4.

(35) Seto, R.; Mari, R.; Morris, J. F.; Denn, M. M. Discontinuous Shear Thickening of Frictional Hard-Sphere Suspensions. *Phys. Rev. Lett.* **2013**, *111*, 218301–1–5.

(36) Lootens, D.; van Damme, H.; Hémar, Y.; Hébraud, P. Dilatant Flow of Concentrated Suspensions of Rough Particles. *Phys. Rev. Lett.* **2005**, *95*, 268302–1–4.

(37) Wyart, M.; Cates, M. E. Discontinuous Shear Thickening without Inertia in Dense Non-Brownian Suspensions. *Phys. Rev. Lett.* **2014**, *112*, 098302–1–5.

(38) Ven, T. G. M. V. D. *Colloidal Hydrodynamics*; Academic Press: London, 1989.

(39) Iskakova, L. Y.; Zubarev, A. Y. Shear Thickening of Dense Suspensions due to Energy Dissipation in Lubrication Layers between Particles. *Phys. Rev. E* **2013**, *88*, 032303-1-6.

(40) Zhao, Y.; Davis, R. H. Interaction of Two Touching Spheres in a Viscous Fluid. *Chem. Eng. Sci.* **2002**, *57*, 1997–2006.

(41) Chellamuthu, M.; Arndt, E. M.; Rothstein, J. P. Extensional Rheology of Shear-Thickening Nanoparticle Suspensions. *Soft Matter* **2009**, *5*, 2117-2124.

(42) Raghavan, S. R.; Walls, H. J.; Khan, S. A. Rheology of Silica Dispersions in Organic Liquids: New Evidence for Solvation Forces Dictated by Hydrogen Bonding. *Langmuir* **2000**, *16*, 7920–7930.

(43) Raghavan, S. R.; Khan, S. A. Shear-Thickening Response of Fumed Silica Suspensions under Steady and Oscillatory Shear. *J. Colloid Interface Sci.* **1997**, *185*, 57–67.

(44) Negi, A. S.; Osuji, C. O. New Insights on Fumed Colloidal Rheology—shear Thickening and Vorticity-Aligned Structures in Flocculating Dispersions. *Rheol. Acta* **2008**, *48*, 871–881.

(45) Crawford, N. C.; Williams, S. K. R.; Boldridge, D.; Liberatore, M. W. Shear-Induced Structures and Thickening in Fumed Silica Slurries. *Langmuir* **2013**, *29*, 12915–12923.

(46) Barthel, H.; Rösch, L.; Weis, J. Fumed Silica-Production, Properties, and Applications. *Organosilicon Chem. Set Mol. Mater.* **1996**, 761–778.

(47) Mathias, J.; Wannemacher, G. Basic Characteristics and Applications of Aerosil: 30. The Chemistry and Physics of the Aerosil Surface. *J. Colloid Interface Sci.* **1988**, *125*, 61–68.

(48) *Technical Bulletin Fine Particles 11:Basic Characteristics of AEROSIL® Fumed Silica*; Evonik Industries.

(49) O'Brie, V. T.; Mackay, M. E. Stress Components and Shear Thickening of Concentrated Hard Sphere Suspensions. *Langmuir* **2000**, *16*, 7931–7938.

(50) Jiang, T.; Zukoski, C. F. Role of Particle Size and Polymer Length in Rheology of Colloid–Polymer Composites. *Macromolecules* **2012**, *45*, 9791–9803.

(51) Glomann, T.; Hamm, A.; Allgaier, J.; Hübner, E. G.; Radulescu, A.; Farago, B.; Schneider, G. J. A Microscopic View on the Large Scale Chain Dynamics in Nanocomposites with Attractive Interactions. *Soft Matter* **2013**, *9*, 10559–10571.

(52) Kim, S. Y.; Meyer, H. W.; Saalwächter, K.; Zukoski, C. F. Polymer Dynamics in PEG-Silica Nanocomposites: Effects of Polymer Molecular Weight, Temperature and Solvent Dilution. *Macromolecules* **2012**, *45*, 4225–4237.

(53) Kumar, S. K.; Jouault, N.; Benicewicz, B.; Neely, T. Nanocomposites with Polymer Grafted Nanoparticles. *Macromolecules* **2013**, *46*, 3199–3214.

(54) Rubenstein, M.; Colby, R. H. *Polymer Physics*; Oxford Univ. Press: New York, 2003.

(55) He, L.; Hu, Y.; Wang, M.; Yin, Y. Determination of Solvation Layer Thickness by a Magnetophotonic Approach. *ACS Nano* **2012**, *6*, 4196–4202.

(56) Guazzelli, É.; Morris, J. F. *A Physical Introduction to Suspension Dynamics*, 1 edition.; Cambridge University Press: Cambridge ; New York, 2012.

(57) Kim, S.; Karrila, S. J. *Microhydrodynamics: Principles and Selected Applications*, Unabridged edition.; Dover Publications: Mineola, N.Y, 2005.

(58) Frankel, N. A.; Acrivos, A. On the Viscosity of a Concentrated Suspension of Solid Spheres. *Chem. Eng. Sci.* **1967**, *22*, 847–853.

(59) Vincent, B.; Edwards, J.; Emmett, S.; Jones, A. Depletion Flocculation in Dispersions of Sterically-Stabilised Particles ("soft Spheres"). *Colloids Surf.* **1986**, *18*, 261–281.

(60) Jiang, W.; Gong, X.; Xu, Y.; Xuan, S.; Jiang, W.; Zhu, W.; Li, X.; Qin, L. Investigating the Confining Compressibility of STF at High Deformation Rate. *Eur. Phys. J. Appl. Phys.* **2012**, *60*, 31101–1 –7.

(61) Maranzano, B. J.; Wagner, N. J. Thermodynamic Properties and Rheology of Sterically Stabilized Colloidal Dispersions. *Rheol. Acta* **2000**, *39*, 483–494.

(62) Bugnicourt, E.; Galy, J.; Gérard, J.F.; Boué, F.; Barthel, H. Structural Investigations of Pyrogenic Silica–Epoxy Composites: Combining Small-Angle Neutron Scattering and Transmission Electron Microscopy. *Polymer* **2007**, *48* (4), 949-958.

(63) Hurd, A. J.; Schaefer, D.W.; Glines, A.M. SANS Study of Sintering of Rough Surfaces. *Journal of Applied Crystallography* **1988**, *21* (6), 864-869.

(64) Beaucage, G.; Ulibarri, T. A.; Black, E. P.; Schaefer, D. W. Multiple Size Scale Structures in Silica Siloxane Composites Studied by Small Angle Scattering. In *Hybrid Organic-Inorganic Composites ACS Symposium Series 585;* Mark, J. E.; Lee, C. Y.; Bianconi, B. A. Ed.; American Chemical Society: Washington DC, 1994.

(65) Geissler, E.; Hecht, A.M.; Rochas, C.; Horkay, F.; Bley, F.; Livet, F., 2002, November. Structure and Dynamics of Silica-filled Polymers by SANS and Coherent SAXS. In *Macromolecular Symposia* **2002**, *190* (1), 23-32.

(66) Koga, T.; Takenaka, M.; Aizawa, K.; Nakamura, M.; Hashimoto, T. Structure Factors of Dispersible Units of Carbon Black Filler in Rubbers. *Langmuir* **2005,** *21* (24), 11409-11413.

(67) Narayanan, R.A.; Thiyagarajan, P.; Zhu, A.J.; Ash, B.J.; Shofner, M.L.; Schadler, L.S.; Kumar, S.K.; Sternstein, S.S. Nanostructural Features in Silica–Polyvinyl Acetate Nanocomposites Characterized by Small-angle Scattering. *Polymer* **2007**, *48* (19), 5734-5741.

(68) Ando, M.; Kawaguchi, M. Shear-Induced Changes in Rheological Reponses and Neutron Scattering Properties of Hydrophobic Silica Suspensions at Low Silica Concentrations. *Journal of Dispersion Science and Technology* **2011**, *32* (5), 686-691.

(69) Butera, R.J.; Wolfe, M.S.; Bender, J.; Wagner, N.J. Formation of a Highly Ordered Colloidal Microstructure Upon Flow Cessation from High Shear Rates. *Physical review letters* 1996, *77* (10), 2117.

(70) Newstein, M.C.; Wang, H.; Balsara, N.P.; Lefebvre, A.A.; Shnidman, Y.; Watanabe, H.; Osaki, K.; Shikata, T.; Niwa, H.; Morishima, Y. Microstructural Changes in a Colloidal Liquid in the Shear Thinning and Shear Thickening Regimes. *The Journal of chemical physics*, **1999**, *111* (10), 4827-4838.

(71) Laun, H.M.; Bung, R.; Hess, S.; Loose, W.; Hess, O.; Hahn, K.; Hädicke, E.; Hingmann, R.; Schmidt, F.; Lindner, P. Rheological and Small Angle Neutron Scattering Investigation of Shear-induced Particle Structures of Concentrated Polymer Dispersions Submitted to Plane Poiseuille and Couette Flow. *Journal of Rheology*, **1992**, *36* (4), 743-787.

(72) Egres, R.G.; Nettesheim, F.; Wagner, N.J. Rheo-SANS Investigation of Acicular-Precipitated Calcium Carbonate Colloidal Suspensions Through the Shear Thickening Transition. *Journal of Rheology*, **2006**, *50* (5), 685-709.

(73) Schaefer, D. W.; Hurd, A. J. Growth and Structure of Combustion Aerosols: Fumed Silica. *Aerosol Science and Technology*, **1990**, *12* (4), 876-890.

(74) Gamez-Corrales, R.; Berret, J.F.; Walker, L.M.; Oberdisse, J. Shear-thickening Dilute Surfactant Solutions: Equilibrium Structure as Studied by Small-angle Neutron Scattering. *Langmuir*, **1999**, *15* (20), 6755-6763.

(75) Kawaguchi, M.; Mizutani, A.; Matsushita, Y.; Kato, T. Molecular Weight Dependence of Structures and Rheological Properties for Fumed Silica Suspensions in Polystyrene Solutions. *Langmuir*, **1996**, *12* (26), 6179-6183.

(76) Hammouda, B *Probing Nanoscale Structures – The SANS Toolbox,* NIST Center for Neutron Research: Gaithersburg, 2016.

(77) Kimura, K.; Kawaguchi, M.; Suzuki, J.; Funahashi, S.; Izumi, Y.; Small Angle Neutron Scattering Study of Silica Suspensions. In *Proceedings of the Fifth International Symposium on Advanced Nuclear Energy Research*; 1994, 647-652.